OPTIMUM DESIGN OF SIMPLICIAL UNIAXIAL ACCELEROMETERS

Simon Desrochers

Department of Mechanical Engineering
McGill University, Montréal

January 2009

A Thesis submitted to the Faculty of Graduate Studies and Research
in partial fulfilment of the requirements for the degree of
Master of Engineering

Abstract

This thesis reports on the design, analysis and optimization of an accelerometer. This accelerometer is designed as a monolithic structure along the concept of compliant mechanisms. An elastodynamic analysis is performed on the compliant mechanism to asses the performance of the inertial sensor.

This thesis proposes an innovative compliant hinge intended to stiffen the structure of compliant mechanisms. In addition, a procedure for the optimum design of this new hinge is discussed. The structural optimization problem is approached by coupling a finite element model to an optimization algorithm. A procedure is developed to generate the mesh at each optimization step according to the values of the design parameters provided by the optimization algorithm. The objective function to minimize is the stress concentration in a hinge loaded under bending.

The last chapter focuses on the multi-objective optimization of the compliant-mechanism accelerometer. The Pareto method is used to optimally design the accelerometer. The purpose is to maximize the sensitivity of the accelerometer in its sensing direction, while minimizing its sensitivity in all other directions. The a posteriori multi-objective optimization is formulated. By using the normalized normal constrained method (NNCM), an even distribution of the Pareto frontier is found. The work also provides several optimum solutions of the Pareto plot as well as the CAD model of the selected solution.

Résumé

Une large gamme d'accéléromètres est offerte sur le marché. Cependant, la plupart des architectures de capteurs inertiels offerts par l'industrie sont constituées d'une masse suspendue par une poutre encastrée. Avec les années, les chercheurs ont mis au point des architectures parallèles offrant une bien meilleure rigidité qu'une simple poutre encastrée. Les accéléromètres à architecture parallèle offrent également de bien meilleures rigidités.

Cette thèse porte sur la conception, l'analyse et l'optimisation d'un accéléromètre à architecture parallèle. Tout d'abord, l'accéléromètre est réalisé comme structure monolithique dans le cadre des mécanismes flexibles. Par la suite, une analyse elasto-dynamique est effectuée sur le mécanisme flexible afin de d'évaluer les performances du capteur inertiel.

Cette thèse propose également une nouvelle articulation flexible visant à améliorer la structure des mécanismes flexibles. Une procédure optimisant le profil de cette nouvelle articulation flexible est également proposée. Le problème d'optimisation structurelle est abordé en établissant une boucle entre un modèle par éléments finis et un algorithme d'optimisation. Une procédure a été développée afin de générer le maillage à chaque étape d'optimisation en fonction des valeurs des paramètres de conception fournis par l'algorithme d'optimisation. La fonction cible à minimiser est définie comme la concentration de contrainte générée dans l'articulation flexible sollicitée en flexion.

Le dernier chapitre de la thèse met l'accent sur l'optimisation multi-objectif du mécanisme flexible de l'accéléromètre. La méthode est utilisée afin d'obtenir la configuration optimale de l'accéléromètre. Le but est de maximiser la sensibilité de l'accéléromètre dans la direction de l'axe sensible, tout en réduisant la sensibilité dans toutes les autres directions. Une formulation de l'optimisation a posteriori des objectifs est présentée. En utilisant la méthode normalisée contrainte (NNCM), une répartition uniforme de la frontière de Pareto est produite. Les solutions optimales de Pareto sont présentées dans un graphique, ainsi que le modèle CAO de la solution sélectionnée.

Acknowledgements

I would like to express my most sincere gratitude to my supervisors, Professors Jorge Angeles and Damiano Pasini, for their guidance and financial support throughout the course of this research. I am specially grateful for all their scientific insights and their careful reviews of the manuscript of this thesis. I would also like to thank Irène Cartier for her help and support with the administrative side of my studies. I thank my colleagues from the Centre of Intelligent Machines and the Multi-scale Design Optimization Group, with whom I had a great time during my studies at McGill University. Special thanks to Mostafa Yourkhani for teaching me Ansys; and to Philippe Cardou and Hossein Ghiasi for their availability, scientific insights and advice. I also want to thank Philippe for all his support during my first moments here at McGill. Many thanks to my friend Jean-Francois Gauthier, for his support during the completion of this thesis. I am also grateful to Jean-Francois for the precious introduction he gave me on LaTeX to start writing the manuscript of this thesis. Last but not least, deep thanks to my family for their love and their encouragement.

TABLE OF CONTENTS

Abstract i

Résumé iii

Acknowledgements v

LIST OF FIGURES xi

LIST OF TABLES xv

CHAPTER 1. Introduction 1
- 1.1. General Background 1
  - 1.1.1. Accelerometer Working Principle 1
  - 1.1.2. Simplicial Architecture for Isotropic Multi-axial Accelerometers . 4
  - 1.1.3. Compliant mechanism 8
- 1.2. Motivation and Thesis Objectives 8
- 1.3. Structure of the Thesis 10

CHAPTER 2. Compliant Mechanism Design 11
- 2.1. Characteristics of Compliant Mechanisms 11
  - 2.1.1. Compliant joint 11
  - 2.1.2. Advantages and disadvantages of compliant mechanisms 12
  - 2.1.3. Translation Micro Displacement 14
- 2.2. The Compliant Realization of the 2ΠΠ Architecture 15
- 2.3. Material Selection for Compliant Accelerometers 18

CHAPTER 3. Modal Analysis of the Compliant Accelerometer 23
3.1. Lumped-parameter Model 24
3.1.1. The System State 24
3.1.2. The System Kinetic Energy 25
3.1.3. The System Potential Energy 25
3.1.4. The Mathematical Model of the Compliant Mechanism 30
3.2. Case Study: One-notched Beam System 31
3.3. Case Study: The Compliant 2ΠΠ System 35
3.3.1. Kinetic Energy 35
3.3.2. Potential Energy 37
3.3.3. Mathematical Model 38
3.4. Alternative Layout 39

CHAPTER 4. Shape Optimization of a Corner-filleted Hinge 45
4.1. Lamé Curves 47
4.1.1. Parameterization of Lamé Curves. 49
4.1.2. Curvature of Lamé Curves. 49
4.2. Basic Problem 51
4.3. Structural Optimization Procedure 52
4.3.1. General Scheme 52
4.3.2. Objective Function and Constraints 54
4.4. Optimum Supercircular Fillet 56
4.5. Optimum Superelliptical Fillet 59
4.5.1. Optimization Algorithm 60
4.5.2. Results 60
4.6. Summary and Discussion 62

CHAPTER 5. Optimum Design of a Compliant Uniaxial Accelerometer . . . 63
5.1. The Optimization Methodology 64
5.2. Problem Formulation 65

5.3. Multi-objective Formulation 69
5.4. RESULTS 74
5.5. DISCUSSION 78

CHAPTER 6. Closing Remarks 81
6.1. Conclusions 81
6.2. Recommendations for Future Work 82

BIBLIOGRAPHY 83

LIST OF FIGURES

1.1 Mass-spring system of an accelerometer 2
1.2 Example industrial accelerometers: (a) piezoelectric in shear mode, (b) piezoelectric in flexure mode; and (c) capacitive 3
1.3 Frequency response 4
1.4 The simplicial 2ΠΠ uniaxial accelerometer: (a)top view (b) front view . . . 5
1.5 The simplicial 3ΠΠ biaxial accelerometer 6
1.6 The simplicial $4R\Pi\Pi R$ triaxial accelerometer 7
2.1 Revolute joint: (a) notched beam joint; and (b) standard mechanical revolute joint 12
2.2 Compliant Hinge: (a) corner-filleted hinge; and (b) elliptic flexural hinge; and (c) notched-beam flexural hinge 13
2.3 Revolute compliant hinge subjected to torsional loading 14
2.4 Compliant realization of the Π-joint: (a) with a pair of constant cross-section beams; and (b) with four notched beams 15
2.5 Compliant realization of the Π-joint in a θ posture 16
2.6 The complaint realization of the ΠΠ-leg architecture 17
2.7 The Simplicial 2ΠΠ Uniaxial Accelerometer 17
2.8 Parametrization of the 2ΠΠ Configuration 18
2.9 The S_y/ρ-E/ρ chart (Ashby, 2005) 21

3.1 The ith compliant link attached to the jth rigid link: (a) layout; (b) detail of the definition of $\mathcal{S}_i(s_i)$ 26

3.2 Notched beam: (a) Mass-spring representation; (b) compliant joint 31

3.3 Uniaxial accelerometer: (a) front view; and (b) bottom view 36

3.4 New layout: (a) CAD model; and (b) deformation along the sensitive axis 40

3.5 New layout of the uniaxial accelerometer: (a) left view; and (b) top view . 41

4.1 Corner filleted hinge 46

4.2 Lamé curves for: (a) $\eta = 2$; (b) $\eta = 3$; and (c) $\eta = 4$ 47

4.3 Lamé curves of eq. (4.2) 48

4.4 Lamé curves polar coordinate for $\eta = 4$ 49

4.5 Flexible beam profiles and their corresponding curvature distributions: (a) (b) circular fillets; (c) (d) supercircular fillets; and (e) (f) superelliptical fillets 51

4.6 Geometry of a Lamé-filleted hinge: (a) supercircular filleted hinge; (b) superelliptical filleted hinge; (c) top view of both hinges 52

4.7 Structural model: (a) front view, (b) top view 53

4.8 Meshing of the flexible beam: (a) front view; and (b) zoom-in on the fillet 55

4.9 Stress concentration factor as a function of power η of a Lamé curve for supercircular fillet 57

4.10 Von Mises stress distribution with (a) no fillet; (b) circular fillet; and (b) optimum supercircular fillet with $\eta = 3.2$ 58

4.11 Link between Matlab and Ansys 61

4.12 Von Mises stress concentration distribution of the optimum super elliptical fillet 62

5.1 Methodology flow chart 66

5.2 Parameterization of the cross-configuration mechanism 67

5.3 FE model of the accelerometer 69

5.4 Structural model 69
5.5 Bi-objective design space 70
5.6 Pareto frontier 71
5.7 Normalized pareto frontier 72
5.8 Pareto frontier 76
5.9 Optimum accelerometer 77
5.10 Von Mises stress distribution 77

LIST OF TABLES

2.1 Material 22

3.1 Dimensions of the one notched-beam system 32

3.2 Modal analysis of one notched beam system 34

3.3 Natural frequencies 34

3.4 Dimensions of the 2ΠΠ system 35

3.5 Modal frequencies and modal vectors of the compliant 2ΠΠ mechanism . 43

3.6 Dimensions of the new layout 44

3.7 Modal analysis of the new layout 44

4.1 Initial values of the parameters for corner-filleted hinge 56

4.2 Summary of results 62

5.1 Pareto solutions 75

5.2 Sensitivity of the accelerometer 77

CHAPTER 1

Introduction

Accelerometers are inertial sensors which provide an output proportional to acceleration. These sensors can be extensively applied in industry. In addition to the technical test measurement and modal analysis, accelerometers are now commonly used in many fields such as the automotive industry, aeronautical and astronautical industry, military industry, robotics systems and medical instruments, video cameras, free-space pointers, and so on (Macdonald, 1990). For example, accelerometers are used in automobile crash tests or guidance systems. Guidance systems made of accelerometers are called Inertial Navigation System (INS).

1.1 General Background

1.1.1 Accelerometer Working Principle. The vast majority of accelerometers function on the principle of the mass-spring system. The mass, referred to as the proof-mass or seismic mass, is elastically suspended on the accelerometer frame. The elastic suspension is realized by means of flexible beams or compliant hinges. Regarding uniaxial accelerometers, the resulting compliant mechanism is designed to allow the proof-mass to translate exclusively along one direction. This is referred to as the sensitive direction. Figure 1.1 represents the mass-spring system of a uniaxial accelerometer where the sensitive direction is that of the x-axis. The resulting proof-mass displacement yields a signal that is linearly related to the acceleration

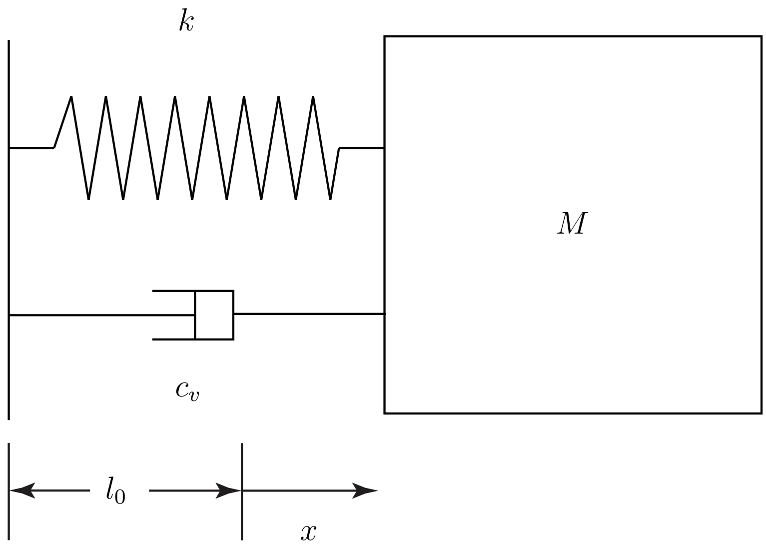

FIGURE 1.1. Mass-spring system of an accelerometer

component in the sensitive direction. It is common practice to refer to the sensitive direction as the *"sensitive axis"*.

The bias errors of inertial measurements come from the off-axis sensitivity of the mechanisms (Senturia, 2001). From a mechanical viewpoint, off-axis sensitivity corresponds to the parasitic motion when the accelerometer is subjected to angular acceleration, or when acceleration is not parallel to the sensitive axis. Therefore, in order to reduce the bias errors, the off-axis stiffness of the proof-mass suspension must be increased.

Various types of accelerometers offering a wide range of properties are available on the market. However, most inertial sensor mechanism found in the industry are made up of a mass suspended by one cantilever beam acting as spring. For example, the low-frequency accelerometers shown in Figs. 1.2a, b and c are, respectively, a uniaxial piezoelectric accelerometer in shear mode, a uniaxial piezoelectric accelerometer in flexural mode, and a capacitive accelerometer (Senturia, 2001; Bao, 2000). Piezoelectric accelerometers are named after the piezoelectric material of their flexural elements. These materials generate an electric potential in response to applied mechanical stress. On the other hand, capacitive accelerometers sense a change in

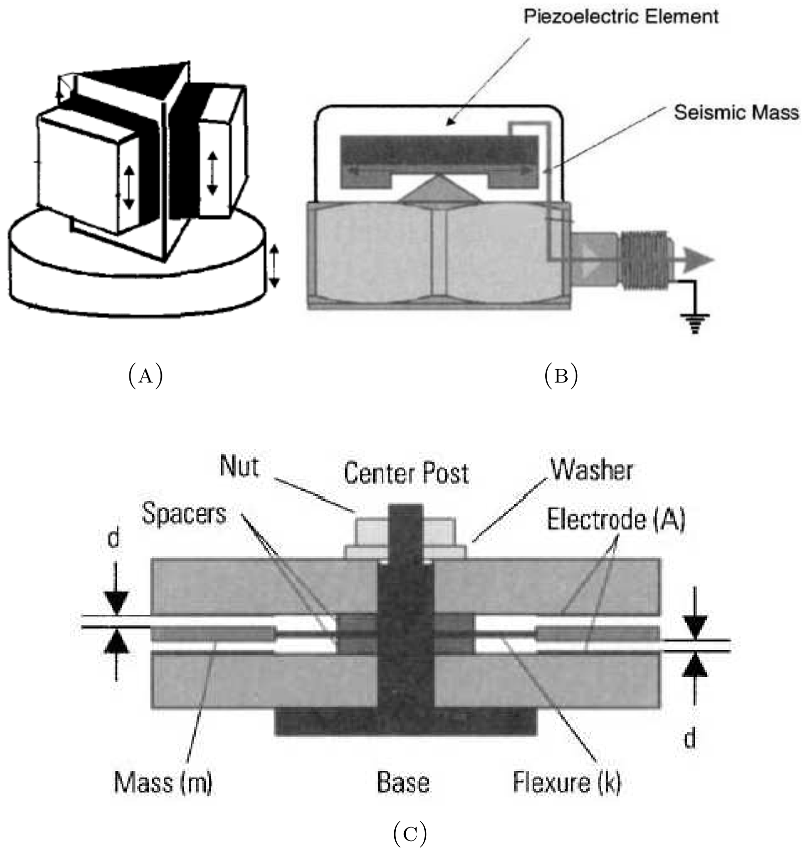

FIGURE 1.2. Example industrial accelerometers: (a) piezoelectric in shear mode, (b) piezoelectric in flexure mode; and (c) capacitive

electrical capacitance with respect to acceleration. Despite the different technologies, all three accelerometers have at least one proof-mass suspended by flexural beams.

The frequency range of accelerometers is quite broad, extending from a few Hertz to several kilohertz. The high-frequency response is limited by the resonance of the seismic mass of the accelerometer spring-mass system. This resonance produces a very high peak in response to the natural frequency λ_n, which is usually somewhere near 1000 Hz for low frequency accelerometers (Fig. 1.3). Accelerometers are ordinarily usable up to about 1/3 of their natural frequency (Senturia, 2001). Data above this frequency will be accentuated by the resonant response, but may be used

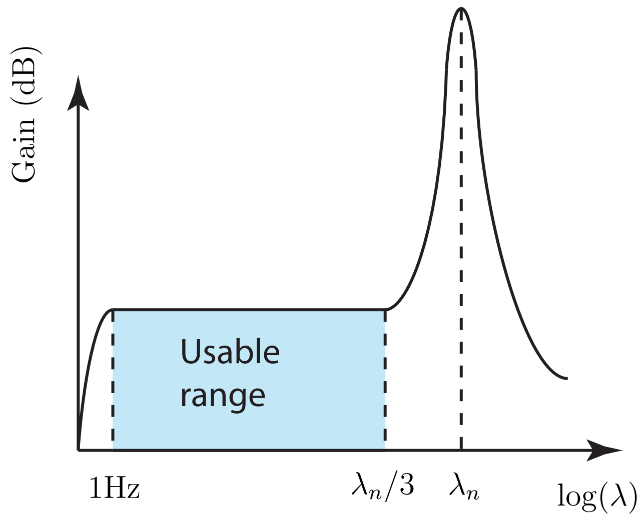

FIGURE 1.3. Frequency response

if the effect is taken into consideration. Since the usable frequency range of low-frequency accelerometers runs from 0 to 600 Hz, the natural frequency should not exceed 1800 Hz.

Low-frequency accelerometers have the advantage of high sensitivity (Navid et al., 2003; Suna et al., 2008). Nonetheless, they have very fragile mechanical structures and high off-axis sensitivity. Consequently, commonly used low frequency accelerometers have a limited range of acceleration, and an off-axis sensitivity of approximately 5%. To override the low off-axis stiffness of serial architectures, researchers have developed parallel architectures offering superior properties compared to a simple cantilever beam.

1.1.2 Simplicial Architecture for Isotropic Multi-axial Accelerometers.

Multi-axis accelerometers currently available on the market are layouts of multiple uniaxial accelerometers that measure acceleration components in orthogonal directions of multiple distinct points of a rigid body. Many efforts have been made to meet the market requirements (Kruglick et al., 1998; Li et al., 2007; Mineta et al., 1996, Puers and Reyntjens, 1998, Algrain and Quinn, 1993, Navid et al., 2003). However, the accelerometers found in the literature have anisotropic mechanical architectures,

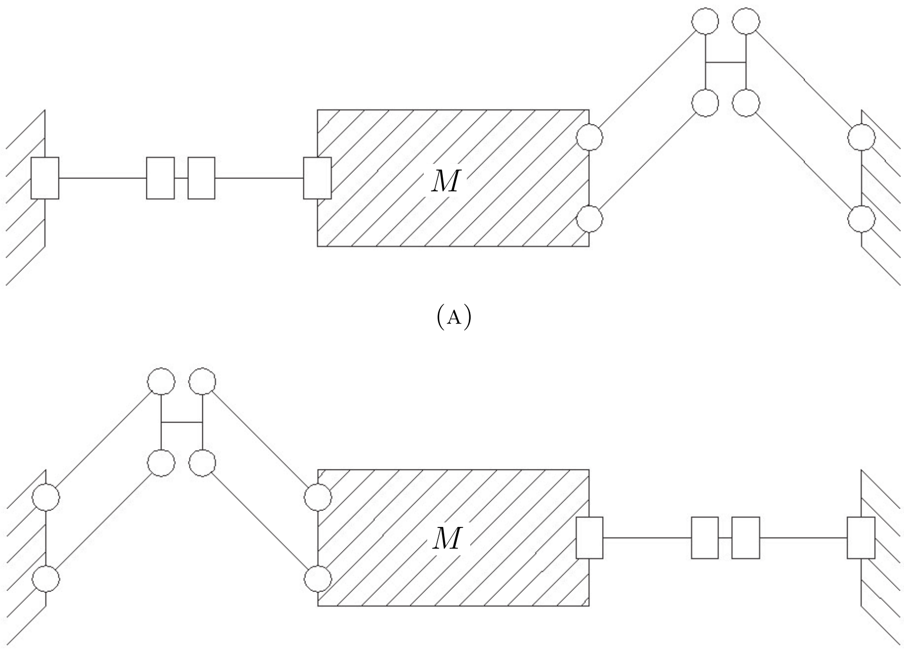

FIGURE 1.4. The simplicial 2ΠΠ uniaxial accelerometer: (a)top view (b) front view

which make them sensitive to parasitic angular acceleration effects. Regarding accelerometers, isotropic mechanical architecture implies that the dynamic properties of the sensor are the same in all directions.

The simplicial architecture for multi-axial accelerometers, proposed by Cardou and Angeles (2007) refers to isotropic mechanism architectures proper of parallel-kinematics machines (PKMs), allowing the measurement of one, two or three acceleration components. Here, Cardou and Angeles (2007) characterize the architecture as simplicial since the proof mass is suspended by $n+1$ legs, where n is the number of acceleration components measured by the accelerometer, with $n = 1, 2, 3$. The set of $n+1$ legs form the vertices a simplex created by the leg attachment points of the n-dimensional accelerometer. Recall that in mathematical programming, a simplex is a polyhedron with the minimum number of vertices embedded in $\mathbb{R}^n$ (Kreyszig, 1997). The polyhedra corresponding to one, two and three dimension are the line, the triangle and the tetrahedron. If the triangle and the tetrahedron are equilateral, then the

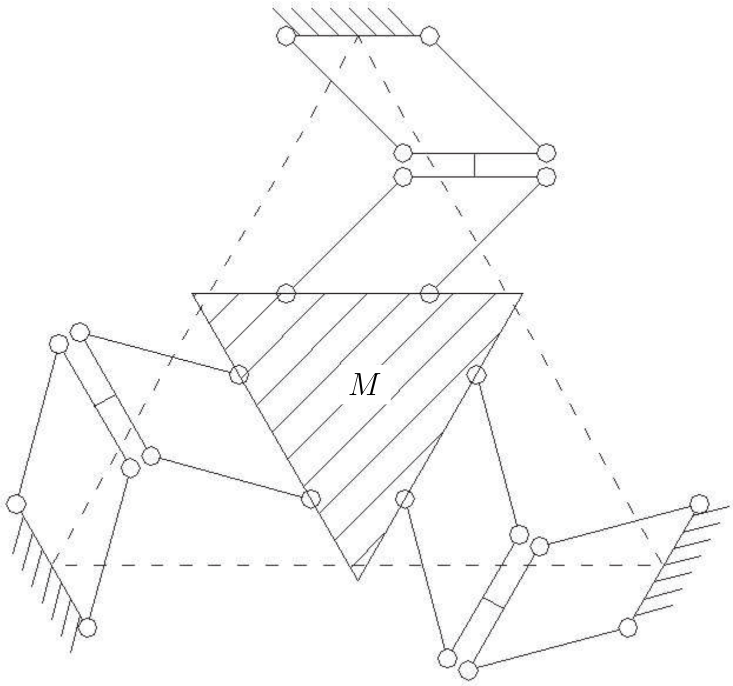

FIGURE 1.5. The simplicial 3ΠΠ biaxial accelerometer

accelerometer is equally sensitive in all the sensitive directions, therefore making the accelerometer isotropic. Furthermore, the accelerometers always have one more leg then dimension, thereby providing redundancy, which considerably adds robustness against measurement error.

The Simplicial Uniaxial Accelerometer (SUA) at hand is intended to measure point-acceleration along one direction (Cardou and Angeles, 2007). To constrain the mass to move along a single axis, we use a ΠΠ-leg architecture, where a Π joint is a parallelogram linkage as described in detail in Angeles (2004). A planar translation mechanism can be obtained by coupling two Π-joints together. The intersection of the two leg-planes forms the new one-dimensional motion line of the mechanism. Therefore, suspending the proof-mass to each leg on both vertices (Fig. 1.4) allows the one-dimensional motion of the proof-mass. In order to eliminate the parasitic displacement due to gravity, each leg-plane is oriented at 45° with respect to the vertical.

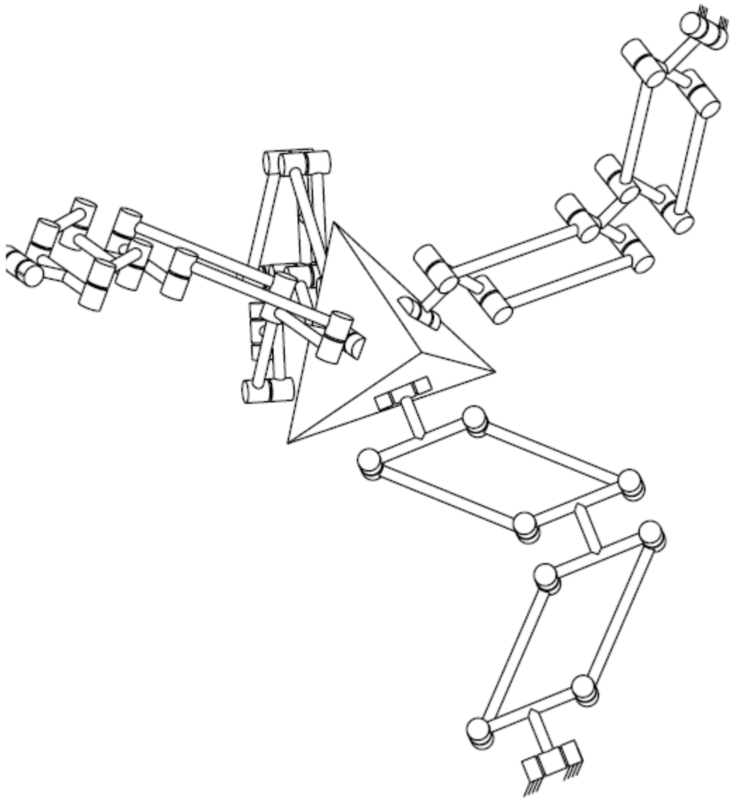

FIGURE 1.6. The simplicial $4R\Pi\Pi R$ triaxial accelerometer

By laying out three ΠΠ-legs in a common plane, symmetrically distributed as show in Fig. 1.5, that is, along the three medians of an equilateral triangle, we obtain the configuration of the Simplicial Biaxial Accelerometer (SBA). This mechanism allows translation in the common plane, while providing a high stiffness in a direction normal to the plane.

The Simplicial Triaxial Accelerometer (STA) is a parallel-robot architecture generating pure translations of the platform with respect to the base. In order to generate pure translations we replace the ΠΠ-legs of the previews architecture by that of the legs of the Japan Mechanical Engineering Laboratory (MEL) Micro Finger (Arai et al., 1996). The architecture shown in Fig. 1.6 is also made of a regular tetrahedron which plays the role of the moving platform, used here as a proof-mass.

1.1.3 Compliant mechanism. Humankind has always been inspired by nature, which is particularly true in engineering. However, human and nature have different design philosophies. For Ananthasuresh and Kota (1995), the crucial difference between natural and human designs lies in a different design paradigm. Traditionally, human-made mechanisms are designed to be strong and rigid, as opposed to the strong and compliant designs of nature. The main point is that rigidity and strength are independent features, and hence, it is possible to make something both compliant and strong. Indeed, *"stiffness is a measure of how much something deflects under a load, whereas strength is how much load can be endured before failure"* (Howell, 2001). Thus, compliant mechanisms follow nature's guidelines by using the compliance properties of materials to store energy and produce work.

Over the years, engineers have learned that assembly plays a major role in production cost. To reduce production cost, compliant mechanisms offer part consolidation; the parts experiencing relative motion are joined together with compliant hinges (Lobontiu, 2003). Before the first publication on the stiffness characterization of compliant hinges by Paros and Weisbord (1965), compliant mechanisms were designed by trial and error. Since than, many studies on compliant hinges have been published (Moon et al., 2002; Lobontiu et al., 2004; Lobontiu and Garcia, 2003; Lobontiu and Garcia, 2005; Stuart et al., 1997; De Bona and Munteanu, 2005; Yingfei and Zhaoying, 2002).

1.2 Motivation and Thesis Objectives

In this thesis, we consider the compliant realization of the Simplicial Uniaxial Accelerometer (SUA). From a fabrication perspective, compliant mechanisms can be classified into two categories. The first category, micromachined mechanisms, is limited to planar mechanisms due to the unidirectional nature of the etching process used in micromachining (Senturia, 2001). The second category comprises the compliant realization of millimeter-scale three-dimensional mechanisms. The complicated geometry of the SUA makes it difficult to manufacture using existing microfabrication techniques. Thus, the second category is contemplated for fabrication of the SUA.

We can cite two main advantages of a compliant realization for the design of accelerometers. First, there is a reduction of the cost as a result of element reduction. Second, the upgraded performance, due to reduced wear, maintenance and weight (Howell, 2001). However, compliant mechanisms have four main drawbacks that can affect the performance of the mechanism: limited sensitivity; off-axis sensitivity; axis drift; and stress concentration (Moon et al., 2002). The sensitivity of the accelerometer is limited by the joint stiffness, which restrains the proof-mass displacement when subjected to acceleration parallel to the sensitive axis. On the other hand, the off-axis sensitivity resulting from the parasitic off-axis bending of the compliant joint should be minimized if the accelerometer is to be insensitive to parasitic off-axis acceleration. The axis drift is governed by the motion precision of the proof-mass. In a device subject to axis-drift, the proof-mass may undesirably move out of its axis of motion. Finally, stress concentration affects the life and the range of motion of the device. The range of motion can be recorded in dimensionless form, according to the *"mechanical advantage"*, which is defined by Lobontiu (2003) as

$$m.a. = \frac{|u_{out}|}{|u_{in}|} \tag{1.1}$$

where u_{in} and u_{out} are the input and output displacement.

Such observations motivate the design of inertial sensors with high resolution and low bias error. The thesis objectives are, hence,

(*i*) The optimum design of a compact compliant uniaxial accelerometer;

(*ii*) the kinematic analysis of lumped compliant accelerometers;

(*iii*) selection of the best configuration of the Simplicial Uniaxial Architecture;

(*iv*) stress analysis of flexible beams; and

(*v*) establishing a design methodology to optimize the stiffness and strength of accelerometers.

1.3 Structure of the Thesis

The remainder of this document is organized as follows. Chapter 2 describes the compliant mechanism design pursued in this project. Chapter 3 provides a detailed description of the lumped-parameter model, as well as its application to different layouts of the SUA. Chapter 4 presents the process used to optimize the compliant hinge. The design process proposed in this work improves the structural properties of compliant hinges by using Lamé-shaped fillets as opposed to the traditional circular fillets. Finally, chapter 5 focuses on the multi-objective optimization of the compliant-mechanism accelerometer. The optimum design of a compact compliant uniaxial accelerometer proposed in this work is the first attempt to use the Pareto multi-objective formulation to optimize accelerometers.

CHAPTER 2

Compliant Mechanism Design

A compliant mechanism is defined by Lobontiu (2003) as *"a mechanism that is composed of at least one flexible component that is sensibly deformable compared to other rigid links"*. Specifically, a compliant mechanism is a device that generates work by using compliant hinges instead of conventional rigid joints. Since flexible hinges do not cause any sliding or rolling, compliant devices are free of backlash and Coulomb friction; however, they are not friction-free, as they are fabricated out of a viscoelastic material that generates viscoelastic forces.

2.1 Characteristics of Compliant Mechanisms

Compliant-mechanism components belong to one of two categories (Cardou et al., 2008). The first category gathers the m compliant links used to transform motion, force, or energy, where m refers to the number of compliant links of the mechanism. The second category comprises the n rigid links designed with low compliance in order to transfer the motion generated by the first category of the components. Here, n refers to the number of rigid links of the compliant mechanism at hand.

2.1.1 Compliant joint. Almost all typical mechanical joints can be replaced by compliant joints; however, the conventional revolute joint is the easiest to replace. A compliant revolute joint, such as those universally described in the works by Paros and Weisbord (1965), Yingfei and Zhaoying (2002), De Bona and Munteanu (2005),

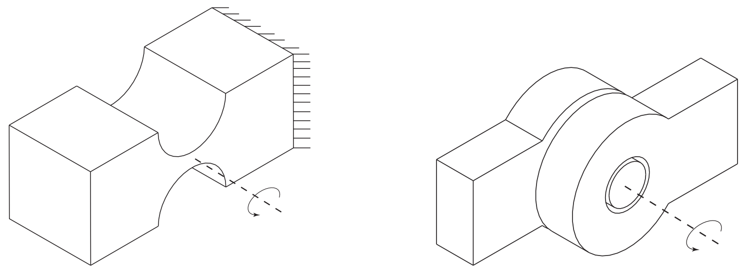

(A) (B)

FIGURE 2.1. Revolute joint: (a) notched beam joint; and (b) standard mechanical revolute joint

and Stuart et al. (1997), is governed by the bending deflection of its cantilever beams. In contrast, the revolute joint in conventional mechanisms is governed by the rolling of bearings or pin joints. A compliant and a standard revolute joint are depicted in Fig. 2.1a and b. Various types of flexural hinges are available to produce compliant revolute joints, all of them using a different beam profile. Typically, only three compliant hinge profiles are found in the literature: the corner filleted hinges (Fig. 2.2a), the elliptic flexural hinge (Fig. 2.2b), and the notched-beam flexural hinges (Fig. 2.2c). Because notched-beam hinges have a good machinability and high off-axis stiffness, we choose notched-beam flexural hinges for the design of the SUA.

2.1.2 Advantages and disadvantages of compliant mechanisms. In general, compliant mechanisms offer several significant advantages compared to conventional mechanisms. In addition to reducing the number of parts to assembly and manufacture, lowering maintenance and miniaturizing the mechanism size, compliant mechanisms are also free of Coulomb friction and backlash, two drawbacks that compromise performance and precision. Typical mechanisms that use bearings or pin-joints always exhibit some degree of parasitic motion and high-frequency noise caused by Coulomb friction. As opposed to compliant mechanisms, bearings and gears with low backlash and low friction are expensive and need lubricant in order to reduce wear between moving parts. Since compliant mechanisms are compact and

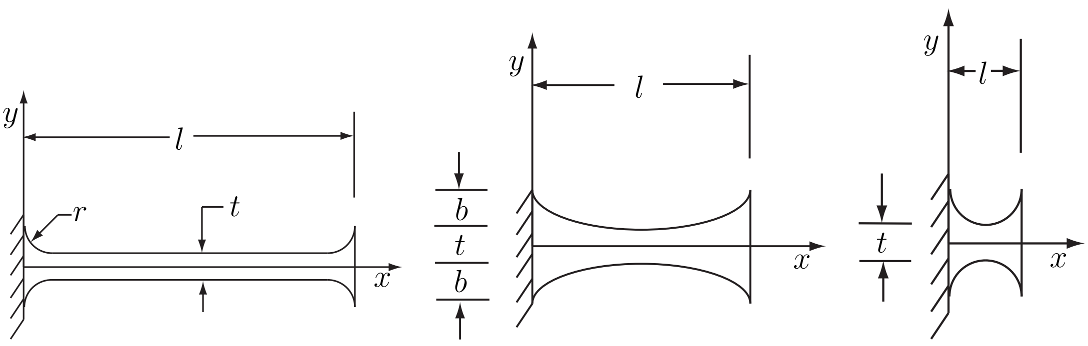

FIGURE 2.2. Compliant Hinge: (a) corner-filleted hinge; and (b) elliptic flexural hinge; and (c) notched-beam flexural hinge

free of backlash and Coulomb friction, they are well suited to precision-mechanism design. Moreover, not needing lubricant, which contributes to their low maintenance, makes them appropriate for clean-environment application.

The advantages of compliant mechanisms come at a price of several drawbacks which can affect the performance of the mechanism. As opposed to typical conventional revolute joints, which have infinite ranges of motion, compliant joints have a limited range of motion that varies depending on the geometry and the material of the compliant joint. Another drawback is the kinematic deficiencies of compliant joints, as studied by Lobontiu and Garcia (2003). More specifically, compliant joints do not have a fixed axis of rotation; rather, their axis of rotation moves along the neutral axis of the compliant beam as the joint is deformed. For their application in accelerometers, the most significant drawback of compliant mechanisms is the poor structural properties manifested when subjected to multi-axis loading. An ideal revolute joint is infinitely rigid in all directions of loading other than that of the axis of rotation. In contrast, a compliant joint always exhibits a degree of stiffness along the desired axis of rotation and a parasitic compliance along all the other axes of loading. For conventional compliant revolute joints, the first parasitic compliance is torsional, as illustrated in Fig. 2.3. It is up to the designer to select an architecture that will reduce the influence of the ratio of stiffness between the sensitive axis and the torsional axis of the compliant joint.

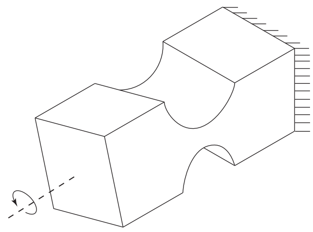

FIGURE 2.3. Revolute compliant hinge subjected to torsional loading

In the case of the compliant realization of the simplicial accelerometer, three main drawbacks affect the performance of the SUA: limited sensitivity in the sensitive direction; off-axis sensitivity; and axis drift. The sensitivity of the accelerometer is limited by the joint stiffness, which restrains the proof-mass displacement when subjected to an acceleration parallel to the sensitive axis. On the other hand, the off-axis sensitivity resulting from the parasitic off-axis bending of the compliant joint should be minimized if the accelerometer is to be insensitive to parasitic off-axis acceleration. Finally, the axis drift is related to the motion precision of the proof-mass. In a device with axis drift problems, the proof-mass may undesirably move out of the sensitive axis.

2.1.3 Translation Micro Displacement. A compliant prismatic pair cannot be design by modifying the shape of a flexible beam, as is the case for revolute joints. In order to realize a prismatic pair, we use Π-joints, whereby two identical straight flexible beams cast at both ends lie parallel to each other to create a parallel-guiding mechanism, or parallelogram, as proposed by Derderian et al. (1996) and depicted in Fig. 2.4a. The resulting mechanism is highly compact but gives only limited off-axis stiffness. To cope with this problem, Arai et al. (1996) proposed a different compliant Π-joint (see Fig. 2.4b), which uses notched beams rather than beams with constant cross-sections. The notched Π-joint brings about higher ratios between the stiffness in the sensitive direction and the stiffness in the other directions. The main drawbacks, as pointed out in Moon et al. (2002), are smaller beam minimum thickness, thereby rendering machining costlier, while giving rise to higher stress concentration, and leading to limited range of motion.

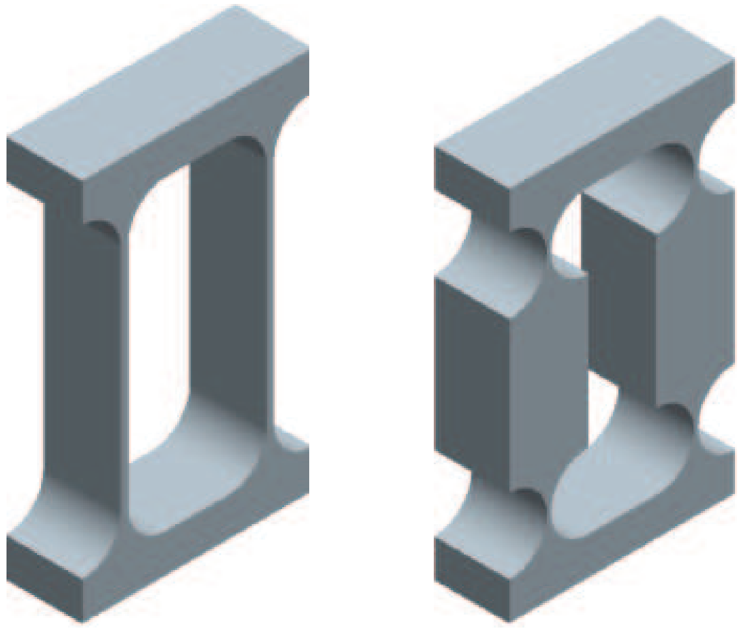

(a) (b)

Figure 2.4. Compliant realization of the Π-joint: (a) with a pair of constant cross-section beams; and (b) with four notched beams

As the mechanism is intended to undergo only small amplitude motion, compliant Π-joints are usually referred to as prismatic joints. In fact, the relative displacement produced is circular translation, which means that all points of one translating line move on circular trajectories of equal radius and different centres with respect to its opposite line. The direction of the equivalent P-joint[1] is given by a circle tangent, the small rotational displacement being considered negligible. By adding an angle θ with respect to the original posture of the Π-joint, we can change the orientation of the direction of the equivalent P pair, as illustrated in Fig 2.5.

2.2 The Compliant Realization of the 2ΠΠ Architecture

By coupling two notched Π-joints in series on the same plane, we obtain a compliant version of the ΠΠ-leg. The layout of Fig. 2.6 has been adopted to produce a two-degree-of-freedom translational system with elastodynamic isotropy, i.e., with its

[1]P denotes a prismatic joint

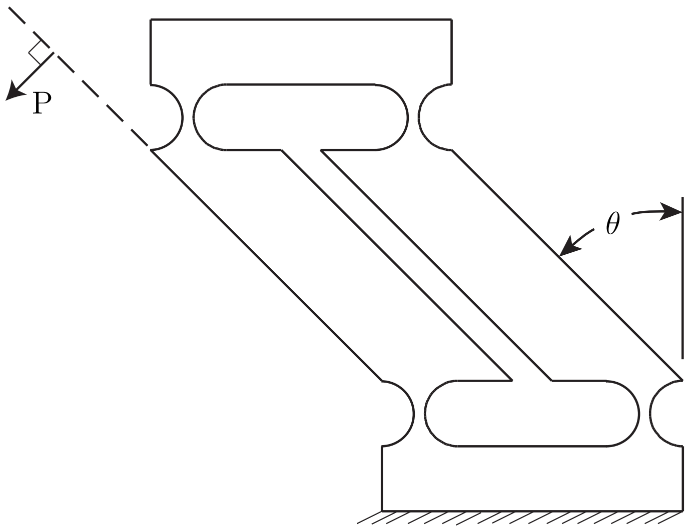

FIGURE 2.5. Compliant realization of the Π-joint in a θ posture

two natural frequencies identical. The resulting ΠΠ-leg is designed with the Π-joint axes at an angle $\theta = 45°$ in the unloaded configuration of the elastic hinges. To create the compliant single-axis simplicial accelerometer, we suspend the proof-mass on two opposite legs, while orienting them so that their respective planes of motion are mutually orthogonal. The resulting device, shown in Fig. 2.7, is a monolithic mechanism that is stiff in the plane normal to the sensitive axis, but compliant in the direction of the latter. This axis is nothing but the intersection of the two leg-planes, the proof-mass thus moves in the direction depicted in Fig 2.7. However, in Chapter 3 we will see that the resulting asymmetric layout generates axis drift and also provides only limited off-axis stiffness. Indeed, as pointed out by Moon et al. (2002), a symmetric layout of compliant joints greatly improves the ratio of the off-axis stiffness to the sensitive-axis stiffness; it also eliminates a major part of the axis drift, which improves the precision in the measurement of the displacement of the proof-mass. Here, it is important to notice the difference between the symmetric layout of compliant hinges and the symmetric profile of a compliant hinge. The first refers to axis of symmetry of compliant mechanism and can be use to ease the kinematic analysis of the system. The second refers to the axis of symmetries of the geometric profile of a given compliant hinge.

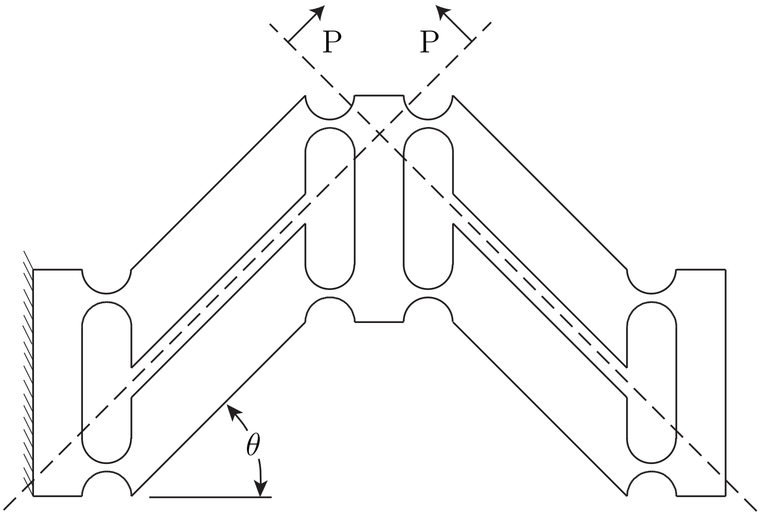

FIGURE 2.6. The complaint realization of the ΠΠ-leg architecture

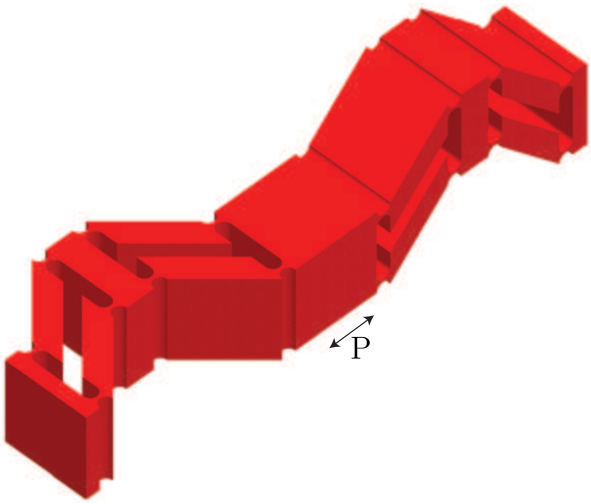

FIGURE 2.7. The Simplicial 2ΠΠ Uniaxial Accelerometer

Eight quantities are needed to parameterize the structure of the SUA, as shown in Fig 2.8. Among those quantities, only three of them are actually parameters of the compliant joints. Parameters l, t, and w are, respectively, the radius, the minimum thickness, and the depth of the joints. Moreover, w represent also the height of the rigid links, including the proof-mass. The remaining five quantities, θ, a, h, b, and e are, respectively, the posture angle of the Π-joint, the length and the height of the rigid links, the thickness of the rigid link coupling the two Π-joints of the legs, and,

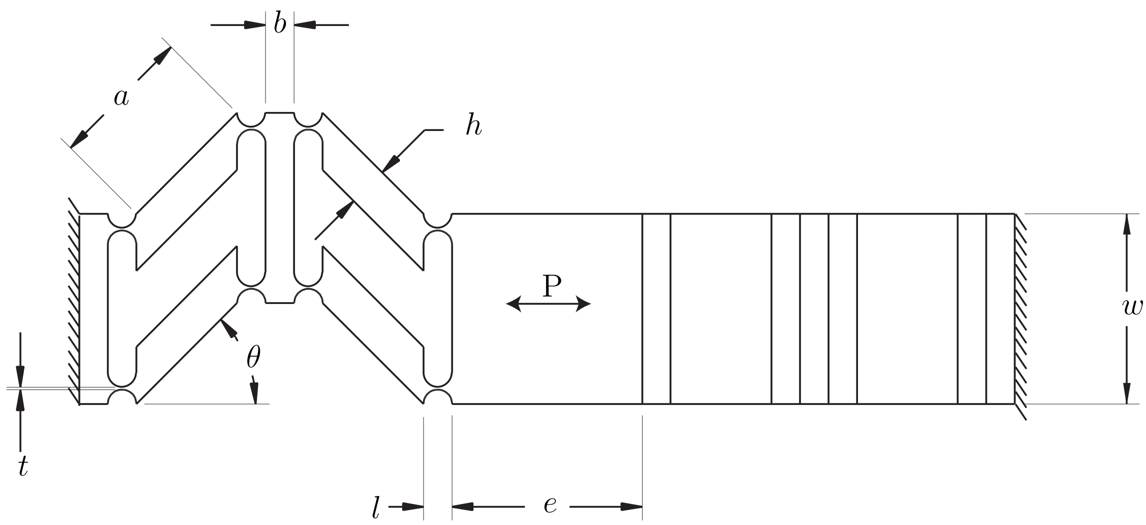

FIGURE 2.8. Parametrization of the 2ΠΠ Configuration

finally, the length of the proof-mass. By setting $e = w$ and $\theta = 45°$ in order to have an inertially[2] isotropic proof-mass and kinetostatically[3] isotropic ΠΠ-legs, the vector $\boldsymbol{x}$ of design variables is defined:

$$\boldsymbol{x} = \begin{bmatrix} a & b & h & w & l & t \end{bmatrix}^T \tag{2.1}$$

To benefit from the precision of the compliant joint and to avoid axis drift, the compliant joints of the SUA are constrained to deformation.

2.3 Material Selection for Compliant Accelerometers

An important issue of compliant-mechanism design is material selection. Here, we consider the compliant joints as springs because the proof mass deflection depends on the bending of its suspending beam. Therefore, the main criterion for material selection of the simplicial accelerometer is related to the primary function of springs, which is to store elastic energy (Ashby, 2005). The elastic energy stored per unit

[2]An inertially rigid body has its three principal moment of inertial identical.
[3]A kinetostatically isotropic compliant mechanism is equally flexible in its sensitive directions.

volume of a spring deformed uniformly under an arbitrary stress σ is

$$V = \frac{1}{2}\Big(\frac{\sigma^2}{E}\Big) \tag{2.2}$$

where E is the material Young Modulus. The spring will be damaged if the stress σ exceeds the yield stress (S_y). The standard measurement of the spring capacity is the modulus of resilience R_m, defined as the energy absorbed by a unit cube of material when loaded in tension to its elastic limits (Juvinall and Marshek, 2000). Thus, R_m is equal to the area under the elastic portion of the stress-strain curve. For a linear spring, we have

$$R_m = \frac{S_y^2}{2E} \tag{2.3}$$

The material density should be minimized to reduce the inertia forces produced by the acceleration of the rigid links. As the inertia forces are the only forces acting on the flexible links, a material with low density improves the range of acceleration of the accelerometer. Here, the range of acceleration is defined by the maximum acceleration possible before plastic deformation occurs in the flexible beams. Therefore, we express the first material criterion for the accelerometer as the ratio of the modulus of resilience R_m and the density ρ. By dropping the constant, we can express the material selection criterion as

$$R_1 = \frac{S_y^2}{\rho E} \tag{2.4}$$

where R_1 corresponds to the criterion selection for light spring as expressed in (Ashby, 2005). The choice of material for light springs is based on the S_y/ρ-E/ρ chart of Fig. 2.9. Candidates of equal performance R_1 are identified by family of lines parallel to the diagonal gray line shown in Fig. 2.9. The materials with highest R_1 are the ones lying at the right of this diagonal gray line. However, since the accelerometer is a monolithic mechanism, the selected material should also give a high stiffness to the rigid links. Indeed, the function of a rigid link is to transfer the elastic deflection of the flexure hinge, without exhibiting any substantial elastic deformation. A material with high Young modulus reduces the parasitic flexion of the rigid link, and thus, the off-axis sensitivity of the accelerometer. Since the material should have a low density to reduce the inertia forces and the stress on the flexible links, we select the specific modulus as second material index, stated as

$$R_2 = \frac{E}{\rho} \tag{2.5}$$

where R_2 is to be maximized. Candidates of equal R_2 values are identified this time by the horizontal grey line shown in Fig. 2.9. The upper right corner formed by the two grey lines, shown in Fig. 2.9, isolates the materials with the best suitable properties. Table 2.1 lists materials typically used in compliant mechanisms. However, some of these materials are discarded because they do not satisfy all the criteria of compliant accelerometers. For example, elastomers offer outstanding properties, but, unfortunately, have the lowest specific modulus of all the materials. Moreover, spring steel is discarded because of its high density. Therefore, by considering only R_1 and R_2 indices, the best choices of materials are carbon fiber reinforced plastic (CFRP), glass fiber reinforced plastic (GFRP), and titanium alloys. To select one of these three materials, we consider other material properties which affect the performance of high-precision instruments. For example, metals have predictable material properties, low susceptibility to creep, and predictable fatigue life. On the contrary, plastics and composites have a large variability in their mechanical properties, making their properties less predictable than those of metals; they are also sensitive to creep and stress relaxation, which could bring some problems in the presence of a constant acceleration such as gravity. For these reasons, we choose to build the accelerometer with the best metal alloy of the S_y/ρ-E/ρ chart (Fig. 2.9) that is a titanium alloy material.

Compliant mechanisms made of titanium alloy may be difficult to manufacture. To cope with this issue, we recourse to the EOSINT M 270 machine tool for Direct Metals Laser-Sintering (DMLS). The machine is designed to manufacture complex

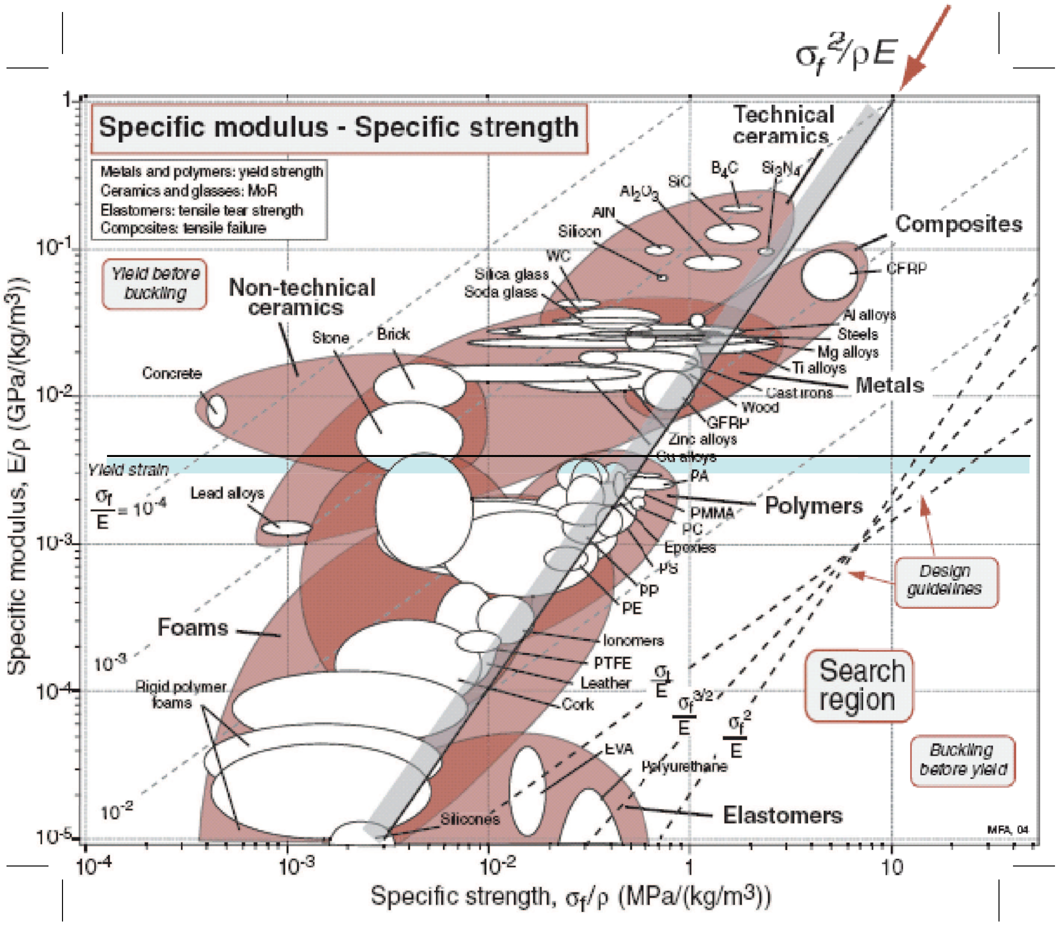

FIGURE 2.9. The S_y/ρ-E/ρ chart (Ashby, 2005)

three-dimensional devices in multiple types of metal, such as stainless steel, tool steel, or, for the case of the accelerometers, TiAl6V4, a titanium alloy. The machine has also an excellent detail resolution of $\epsilon = 100\mu$m, which corresponds to the laser focus diameter. With the precision of the DMLS machine, a monolithic titanium accelerometer can be manufactured in a small size.

Table 2.1. Material

Material	$R_1 = \frac{S_y^2}{E\rho}$	Comment
Spring Steel	0.4-0.9	Poor, because of high density
Ti alloys	0.9-2.6	Metal with the best R_1 criterion; expensive
CFRP	3.9-6.5	Anisotropic material; expensive
GFRP	1.0-1.8	Anisotropic material; less expensive than CFRP
Polymers	1.5-2.5	Low properties predictability
Nylon	1.3-2.1	With low specific modulus E/ρ
Rubber	18-45	With low specific modulus E/ρ

CHAPTER 3

Modal Analysis of the Compliant Accelerometer

The derivations below apply to three-dimensional motion, with a straightforward adaptation for one- and two-dimensional motions. Since the mechanism studied here is intended to measure an inertia force with arbitrary orientation in space, we resort to the general case of three-dimensional beam deflection. Moreover, even if forces and moments acting on the off-axis direction of the moving mass should have a negligible effect on its displacement, we will take it into account, in order to estimate the cross-effects of angular acceleration on the acceleration measurements.

The lumped-parameter model proposed by Cardou et al. (2008) was originally introduced to compute the natural frequencies and the dynamic responses of micro-electromechanical-systems (MEMS). The model is formulated under the assumptions of long Euler-Bernoulli beams and small displacements. However, notched beams do not necessarily respect these assumptions because its strain stress is concentrated in a small region around the centre of rotation. Therefore, before performing the modal analysis of the SUA, we must validate the above mentioned lumped-parameter model, adopted here, for millimeter-scale compliant mechanisms using notched beams.

3.1 Lumped-parameter Model

A compliant mechanism is a chain of components, where each component falls into one of two categories. The first comprises the m compliant links, which are assumed to have no inertia and a given compliance in all directions. The second contains the n rigid links, to which a given inertia and no compliance are assigned.

The compliant links are modeled as Euler-Bernoulli beams, and the deformation of these links is considered to be small. From this last assumption, the mass and stiffness properties of the links are assumed to be constant, that is, independent from the mechanism state.

3.1.1 The System State. Let us first define the fixed frame $\mathcal{F}$, and frames $\mathcal{R}'_j$, $j = 1, \ldots, n$, attached to the j^{th} rigid link. Moreover, we define frame $\mathcal{R}_j$ as the equilibrium pose of the j^{th} rigid body. The origins of frames $\mathcal{F}$, $\mathcal{R}_j$, and $\mathcal{R}'_j$ are labelled O, R_j, and R'_j, $j = 1, ..., n$, respectively. Points R_j, and R'_j are located at the centre of mass of the j^{th} rigid-link. The displacement taking $\mathcal{F}$ into $\mathcal{R}_j$ is described by the pose array $\mathbf{r}_j \equiv [\boldsymbol{\theta}_j^T \quad \boldsymbol{\rho}_j^T]$, where $\boldsymbol{\theta}_j \in \mathbb{R}^3$ is the product $\phi_j \mathbf{e}_j$, with ϕ_j and $\mathbf{e}_j$ denoting the natural invariants of the associated rotation and $\boldsymbol{\rho}_j \equiv \overrightarrow{OR_j} \in \mathbb{R}^3$. The natural invariants of a rotation are the unit-vector $\mathbf{e}_j$ pointing in the axis of rotation, and ϕ_j is the angle of rotation (Angeles, 2007). Notice that, in the presence of small-amplitude rotations, the rotation is fully described by only three independent variables, thereby obviating the need of a four-invariable representation.

Let the displacement of the system frame equilibrium at an arbitrary posture be described by the array $\mathbf{x}$. We define the pose of the j^{th} rigid link with respect to its equilibrium array as

$$\mathbf{x}_j = [\boldsymbol{\nu}_j^T \quad \boldsymbol{\zeta}_j^T]^T \tag{3.1}$$

where $\boldsymbol{\nu}_j \in \mathbb{R}^3$ is the products of the natural invariants ϕ_j and $\mathbf{e}_j$ of the associated rotation taking $\mathcal{R}_j$ into $\mathcal{R}'_j$ and $\boldsymbol{\zeta_j} \in \mathbb{R}^3$ is the vector of the translation displacement. Under the assumption of small-amplitude rotations, only the vector part of the four scalar invariants are needed (Angeles, 2007). Since the posture of the mechanism is fully described by the poses of all the rigid links, we will regard the pose arrays $\mathbf{x}_j, j = 1, \ldots, n$, as the system states. This results in the $6n$-dimensional state vector

$$\mathbf{x} = [\mathbf{x}_1^T \quad \mathbf{x}_2^T \quad \ldots \quad \mathbf{x}_n^T]^T \tag{3.2}$$

3.1.2 The System Kinetic Energy. Let us first store the mass properties of the j^{th} rigid link into its associated mass matrix

$$\mathbf{M}_j \equiv \begin{bmatrix} \mathbf{I}_j & \mathbf{0}_{3\times3} \\ \mathbf{0}_{3\times3} & m_j \mathbf{1}_{3\times3} \end{bmatrix}, \tag{3.3}$$

where $\mathbf{I}_j$, m_j, $\mathbf{0}_{3\times3}$, and $\mathbf{1}_{3\times3}$ are, respectively, the centroidal inertia matrix computed with respect to point R_j of the j^{th}, the mass of the j^{th} rigid link, the 3×3 zero matrix, and the 3×3 identity matrix. Under the assumption of small deformation, the kinetic energy of the system is expressed as

$$T = \frac{1}{2} \sum_{j=1}^{n} \dot{\mathbf{x}}_j^T \mathbf{M}_j \dot{\mathbf{x}}_j = \frac{1}{2} \dot{\mathbf{x}}^T \mathbf{M} \dot{\mathbf{x}}, \tag{3.4}$$

where $\mathbf{M}$ is the $6n \times 6n$ mass matrix of the system, namely,

$$\mathbf{M} \equiv \begin{bmatrix} \mathbf{M}_1 & \mathbf{0}_{6\times6} & \cdots & \mathbf{0}_{6\times6} \\ \mathbf{0}_{6\times6} & \mathbf{M}_2 & \cdots & \mathbf{0}_{6\times6} \\ \vdots & \vdots & \ddots & \vdots \\ \mathbf{0}_{6\times6} & \mathbf{0}_{6\times6} & \cdots & \mathbf{M}_n \end{bmatrix}, \tag{3.5}$$

where $\mathbf{0}_{6\times6}$ is the 6×6 zero matrix.

3.1.3 The System Potential Energy. Consider the i^{th} compliant link that is clamped, at one end, to the j^{th} rigid link, and, at the other end, to the k^{th} rigid link, with $j < k$. From the free-body diagram of the i^{th} compliant link shown in Fig. 3.1, we see that the wrench $\mathbf{v}_i \in \mathbb{R}^6$ applied at the mass centre R_j by the j^{th} rigid link onto the i^{th} compliant link has to be balanced out by wrench $\mathbf{u}_i(s_i) \in \mathbb{R}^6$ applied at the origin

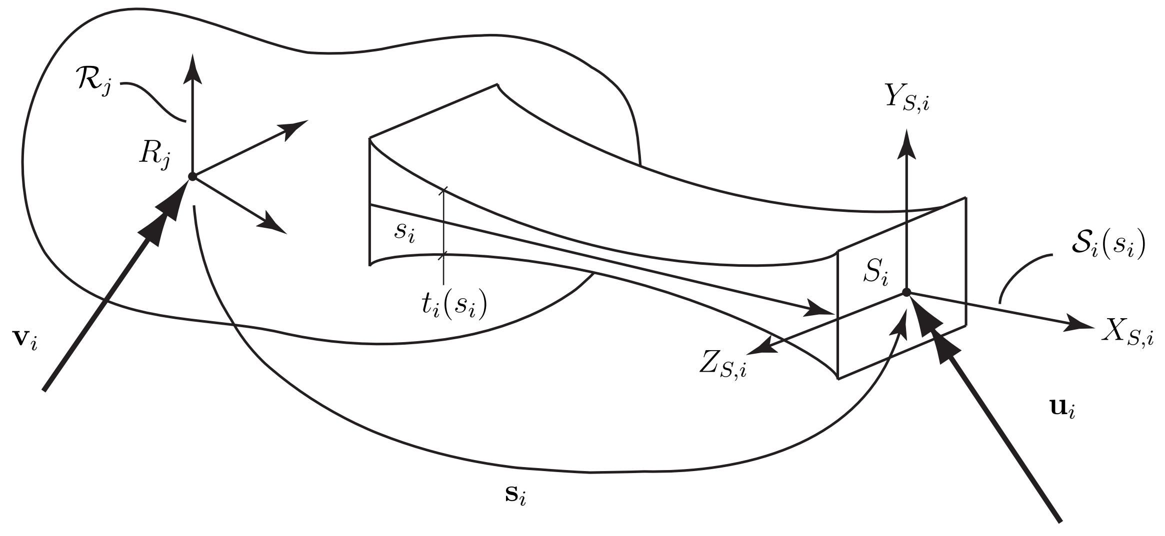

FIGURE 3.1. The ith compliant link attached to the jth rigid link: (a) layout; (b) detail of the definition of $\mathcal{S}_i(s_i)$

of frame $\mathcal{S}_i(s_i)$, S_i, where s_i is a coordinate along the compliant hinge neutral axis. The positive direction of s_i is oriented toward the k^{th} rigid link. The wrenches are defined so that their reciprocal product with the small-displacement screws defined in eq. (3.1) be dimensionally compatible. Therefore, the first three components of the wrench represent a moment, whereas the last three represent a force, the latter applied at the corresponding mass centre, where the wrench is defined. Let us attach frame $\mathcal{S}_i(s_i)$ with axes $X_{S,i}$, $Y_{S,i}$, and $Z_{S,i}$, to the beam cross-section at s_i, as shown in Fig. 3.1 . Frame $\mathcal{S}_i(s_i)$ is defined so as to have its $X_{S,i}$ axis tangent to the beam neutral axis and pointing in the positive direction of s_i, its $Y_{S,i}$ and $Z_{S,i}$ axes defined along the principal directions of the cross-section. Let $\boldsymbol{\tau}(s_i)$ be the array of products of the natural invariants ϕ_j and $\mathbf{e}_j$ of the associated rotation taking frame $\mathcal{R}_j$ into frame $\mathcal{S}_i(s_i)$, following the same convention as that used for $\boldsymbol{\theta}$, and $\boldsymbol{\sigma}_i(s_i) \in \mathbb{R}^3$ be the vector directed from point R_j to point S_i. We group these two arrays in the cross-section pose array defined as

$$\mathbf{s}_i(s_i) \equiv [\boldsymbol{\tau}_i^T(s_i) \quad \boldsymbol{\sigma}_i^T(s_i)]^T \in \mathbb{R}^6. \tag{3.6}$$

The strain energy in a beam element of length ds_i, starting at coordinate s_i and ending at coordinate $s_i + ds_i$, is computed as

$$dU_i(s_i) = (1/2)[\mathbf{u}_i(s_i)]^T_{\mathcal{S},i}\mathbf{H}_i(s_i)[\mathbf{u}_i(s_i)]_{\mathcal{S},i}ds_i, \tag{3.7}$$

where $[\,\cdot\,]_{\mathcal{S},i}$ indicates that the quantity $(\cdot)$ is expressed in frame $\mathcal{S}_i(s_i)$. Matrix $\mathbf{H}_i(s_i) \in \mathbb{R}^6$, in turn, contains the properties of the cross-section. This matrix is defined according to the strain energy formulas for beams (Roark and Young, 1975):

$$\mathbf{H}_i(s_i) \equiv \mathrm{diag}\left(\frac{1}{\mathrm{G_iJ_i}}, \frac{1}{\mathrm{E_iI_{Y,i}}}, \frac{1}{\mathrm{E_iI_{Z,i}}}, \frac{1}{\mathrm{E_iA_i}}, \frac{\alpha_{\mathrm{Y,i}}}{\mathrm{G_iA_i}}, \frac{\alpha_{\mathrm{Z,i}}}{\mathrm{G_iA_i}}\right), \tag{3.8}$$

where E and G are the Young and the shear modulus; $I_{Y,i}$, $I_{Z,i}$ and J_i are the $Y_{S,i}$ axis moment of inertia, the $Z_{S,i}$ axis moment of inertia and the torsional modulus of the beam cross section, respectively; A_i is the area of the cross-section; and $\alpha_{Y,i}$ and $\alpha_{Z,i}$ are the shearing effect coefficients for the $Y_{S,i}$ and $Z_{S,i}$ directions, respectively.

The adjoint $\mathbf{S}_i(s_i)$ of the small-displacement screw $\mathbf{s}_i(s_i)$ is defined as

$$\mathbf{S}_i \equiv \begin{bmatrix} e^{\mathrm{CPM}(\boldsymbol{\tau}_i(s_i))} & \mathbf{0}_{3\times 3} \\ \mathrm{CPM}(\boldsymbol{\sigma}(s_i))e^{\mathrm{CPM}(\boldsymbol{\tau}_i(s_i))} & e^{\mathrm{CPM}(\boldsymbol{\tau}_i(s_i))} \end{bmatrix}, \tag{3.9}$$

where CPM($\cdot$)[1] denotes the cross-product matrix of the three-dimensional vector ($\cdot$). The adjoint $\mathbf{S}_i(s_i)$ leads to the following expression of wrench $[\mathbf{v}]_{\mathcal{R},j}$ in frame $\mathcal{S}_i(s_i)$,

$$[\mathbf{u}_i(s_i)]_{\mathcal{S},i} = -[\mathbf{v}_i]_{\mathcal{S},i} = -\mathbf{S}_i^T[\mathbf{v}_i]_{\mathcal{R},j} \tag{3.10}$$

where the first equality was obtained from the equilibrium in the free-body diagram of Fig. 3.1. Upon substituting eq. (3.10) into eq. (3.7) and integrating over the length

[1] CPM($\mathbf{a}$) is defined as $\partial(\mathbf{a}\times\mathbf{x})/\partial\mathbf{x}$, for any $\mathbf{a}, \mathbf{b} \in \mathbb{R}^3$

of the i^{th} compliant link, we obtain the strain energy as

$$V_i = \frac{1}{2}[\mathbf{v}_i]^T_{\mathcal{R},j}\mathbf{B}_i[\mathbf{v}_i]_{\mathcal{R},j}, \quad \text{where} \quad \mathbf{B}_i \equiv \int_0^{l_i} \mathbf{S}_i(s_i)\mathbf{H}_i(s_i)\mathbf{S}_i(s_i)^T ds_i, \tag{3.11}$$

and l_i is the length of the i^{th} compliant link. To express all the wrenches $\mathbf{v}_i$ in the same reference frame $\mathcal{F}$, the adjoint $\mathbf{R}_j$ of screw $\mathbf{r}_j$ is defined as

$$\mathbf{R}_i \equiv \begin{bmatrix} e^{\mathrm{CPM}(\boldsymbol{\theta}_i)} & \mathbf{0}_{3\times3} \\ \mathrm{CPM}(\boldsymbol{\rho})e^{\mathrm{CPM}(\boldsymbol{\theta}_i)} & e^{\mathrm{CPM}(\boldsymbol{\theta}_i)} \end{bmatrix}, \tag{3.12}$$

which represents the rigid-body motion taking frame $\mathcal{F}$ into frame $\mathcal{R}_j$. Hence, we have the relation

$$[\mathbf{v}_i]_{\mathcal{R},j} = \mathbf{R}_j^T[\mathbf{v}_i]_{\mathcal{F}}, \tag{3.13}$$

and the total strain energy of the system becomes (Cardou, 2007)

$$V = \frac{1}{2}[\mathbf{v}]^T_{\mathcal{F}}\mathbf{B}[\mathbf{v}]_{\mathcal{F}}, \tag{3.14}$$

where $[\mathbf{v}]_{\mathcal{F}} \equiv [[\mathbf{v}_1]^T_{\mathcal{F}} \quad [\mathbf{v}_2]^T_{\mathcal{F}} \quad \cdots \quad [\mathbf{v}_m]^T_{\mathcal{F}} \quad]^T$, and $\mathbf{B}$ is a block-diagonal matrix, its i^{th} block being the 6×6 matrix $\mathbf{R}_j\mathbf{B}_i\mathbf{R}_j^T$, with j taking the value of the smallest index among those of the two rigid links that are connected to the i^{th} compliant link. According to Cardou et al. (2008), the static equilibrium of the wrenches takes the form

$$[\mathbf{w}]_{\mathcal{R}} = \mathbf{R}^T\mathbf{A}[\mathbf{v}]_{\mathcal{F}}, \tag{3.15}$$

where $\mathbf{R}$ is a block-diagonal matrix, its j^{th} block being the 6×6 matrix $\mathbf{R}_j$, while $\mathbf{A}$ is defined as

$$\mathbf{A} \equiv \begin{bmatrix} \mathbf{A}_{11} & \mathbf{A}_{12} & \cdots & \mathbf{A}_{1m} \\ \mathbf{A}_{21} & \mathbf{A}_{22} & \cdots & \mathbf{A}_{2m} \\ \vdots & \vdots & \ddots & \vdots \\ \mathbf{A}_{n1} & \mathbf{A}_{n2} & \cdots & \mathbf{A}_{nm} \end{bmatrix} \in \mathbb{R}^{6n\times6m}, \tag{3.16}$$

with

$$\mathbf{A}_{ji} = \begin{cases} \mathbf{0}_{6\times 6}\ , & \text{if compliant link } i \text{ is not connected to rigid link } j; \\ \mathbf{1}_{6\times 6}\ , & \text{if compliant link } i \text{ is connected to rigid links } j \text{ and } k, \text{ with } j < k; \\ -\mathbf{1}_{6\times 6}\ , & \text{if compliant link } i \text{ is connected to rigid links } j \text{ and } k, \text{ with } j > k. \end{cases} \tag{3.17}$$

This allows the introduction of the potential energy of the external wrenches as a function of the internal wrenches, namely,

$$\Pi = -[\mathbf{w}]_{\mathcal{R}}^T[\mathbf{x}]_{\mathcal{R}} = -[\mathbf{v}]_{\mathcal{F}}^T\mathbf{A}^T\mathbf{R}[\mathbf{x}]_{\mathcal{R}}. \tag{3.18}$$

For a linearly elastic system, the potential energy V and the complementary potential energy $\bar{V}$ take the same value, which is the sum of the strain energy and the potential energy; i.e.,

$$\bar{V} = V = U + \Pi = (1/2)[\mathbf{v}]_{\mathcal{F}}^T\mathbf{B}[\mathbf{v}]_{\mathcal{F}} - [\mathbf{v}]_{\mathcal{F}}^T\mathbf{A}^T\mathbf{R}[\mathbf{x}]_{\mathcal{R}}. \tag{3.19}$$

From eq. (3.19), the problem may now be regarded as that of finding the internal wrenches $\mathbf{v}$ that minimize the complementary potential energy V for a given displacement $\mathbf{x}$ of the rigid links. This follows from the second theorem of Castigliano (Juvinall and Marshek, 2000). The partial derivative of $\bar{V}$ with respect to the internal wrenches yields

$$\frac{\partial\bar{V}}{\partial[\mathbf{v}]_{\mathcal{F}}} = \mathbf{B}[\mathbf{v}]_{\mathcal{F}} - \mathbf{A}^T\mathbf{R}[\mathbf{x}]_{\mathcal{R}} \tag{3.20}$$

whereas the Hessian yields

$$\frac{\partial^2\bar{V}}{\partial[\mathbf{v}]_{\mathcal{F}}^2} = \mathbf{B} \tag{3.21}$$

One may readily verify, from eq. (3.21), that $\mathbf{B}$ is symmetric, positive-definite and, therefore, all stationary points $\mathbf{v}$ of $\bar{V}$ are local minima. Matrix $\mathbf{B}$ being nonsingular, eq. (3.20) admits one single root, namely,

$$[\mathbf{v}]_{\mathcal{F}} = \mathbf{B}^{-1}\mathbf{A}^T\mathbf{R}[\mathbf{x}]_{\mathcal{R}}. \tag{3.22}$$

Upon substituting eq. (3.15) into the foregoing equation, we obtain

$$[\mathbf{w}]_{\mathcal{R}} = \mathbf{K}[\mathbf{x}]_{\mathcal{R}} \qquad \text{where} \quad \mathbf{K} = \mathbf{R}^T\mathbf{A}\mathbf{B}^{-1}\mathbf{A}^T\mathbf{R}. \tag{3.23}$$

The potential energy can now be written as a function of the system posture $\mathbf{x}$, namely,

$$V = \frac{1}{2}\mathbf{x}^T\mathbf{K}\mathbf{x} \tag{3.24}$$

3.1.4 The Mathematical Model of the Compliant Mechanism.

The Lagrangian of the mechanism is readily computed as

$$L = T - V = \frac{1}{2}\dot{\mathbf{x}}^T\mathbf{M}\dot{\mathbf{x}} - \frac{1}{2}\mathbf{x}^T\mathbf{K}\mathbf{x} \tag{3.25}$$

which leads to the Lagrange equation

$$\frac{d}{dt}\left(\frac{\partial L}{\partial \mathbf{x}}\right) - \frac{\partial L}{\partial \dot{\mathbf{x}}} = \mathbf{0}_n \tag{3.26}$$

whence,

$$\mathbf{M}\ddot{\mathbf{x}} + \mathbf{K}\mathbf{x} = \mathbf{0}_n \tag{3.27}$$

As the mass matrix is bound to be symmetric and positive definite, we can express its Cholesky decomposition as $\mathbf{M} = \mathbf{L}\mathbf{L}^T$. This allows us to rewrite eq. (3.27) through the change of variable $\mathbf{z} = \mathbf{L}^T\mathbf{x}$, namely,

$$\ddot{\mathbf{z}} + \mathbf{\Omega}^2\mathbf{z} = 0 \tag{3.28}$$

where $\mathbf{\Omega}^2 = \mathbf{L}^{-1}\mathbf{K}\mathbf{L}^{-T}$ and $\mathbf{\Omega}$ is the system $6n \times 6n$ frequency matrix. Let ω_i and $\boldsymbol{\omega}_i$, $i = 1, \ldots, n$, be the i^{th} eigenvalue and its corresponding eigenvector of $\mathbf{\Omega}^2$, and λ_i and $\boldsymbol{\lambda}_i$ be the i^{th} natural frequency and its corresponding modal vector of the undamped, non-excited system, i.e.,

$$\lambda_i = \sqrt{\omega_i}, \qquad \text{and} \qquad \boldsymbol{\lambda}_i = \mathbf{L}^{-T}\boldsymbol{\omega}_i, \quad i = 1, \ldots, n. \tag{3.29}$$

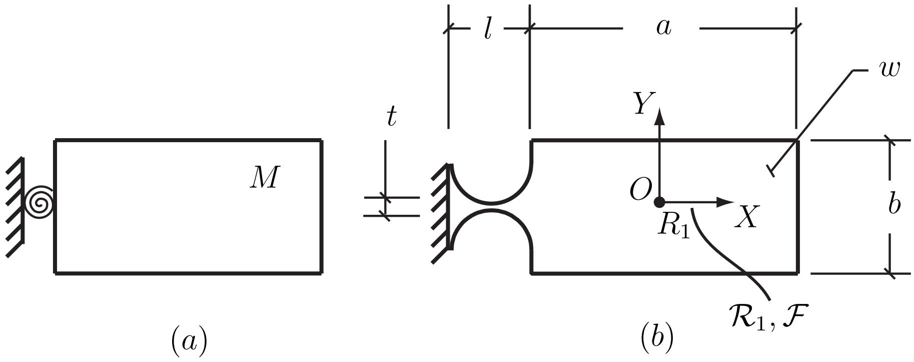

FIGURE 3.2. Notched beam: (a) Mass-spring representation; (b) compliant joint

3.2 Case Study: One-notched Beam System

The one-notched beam system is a compliant version of the spring-mass system depicted in Fig. 3.2. This system is a simple mechanism whose natural frequencies can be readily computed using either a mass-spring system or finite element analysis. Thereupon, this is a good starting point to validate the mathematical model.

The single-degree-of-freedom mechanism acts as a mass-spring system made of one torsional spring and one rigid body in a serial configuration. The first natural frequency of the compliant mechanism should be along the degree of freedom of the mass-spring system. To corroborate this, we analyze the mechanical structure of the compliant mechanism parameterized in Fig. 3.2b. The dept, w, of the mechanism is measured in the direction normal to the plane of the figure. The dimensions of the mechanism studied in this work are recorded in Table 3.1.

Frames $\mathcal{F}$ and $\mathcal{R}_1$ are defined in Fig. 3.2b, with their X axis along the neutral axis of the flexible beam, and with their Z axis oriented in the sensitive direction, which is normal to the plane of the figure. The origins O and R_1 of these two frames are located at the proof-mass centre of mass. Therefore, we have

$$\mathbf{R} = \mathbf{R}_1 = \mathbf{1}_{6\times 6}. \tag{3.30}$$

The mechanism is made of a Titanium alloy, which has a Young Modulus of $E = 117$ GPa, a Poisson ratio of $\mu = 0.33$ and a density of $\rho = 4453$ Kg/m^3. From

TABLE 3.1. Dimensions of the one notched beam system

l	t	w	a	b
3 mm	250 μm	10 mm	10 mm	5 mm

the selected dimension of Table 3.1, the corresponding inertia matrix and mass were estimated to be

$$[\mathbf{I}_1]_{\mathcal{R}_1} = [\mathbf{I}_1]_{\mathcal{F}} = [\mathbf{I}_2]_{\mathcal{R}_2} = \begin{bmatrix} 2.3192 & 0 & 0 \\ 0 & 3.7108 & 0 \\ 0 & 0 & 2.3193 \end{bmatrix} \times 10^{-8} \text{ kg} \cdot \text{m}^2, \tag{3.31}$$

and $m_1 = 2.2265 \times 10^{-3}$ kg. The mass matrix $\mathbf{M}$ is evaluated directly from these numerical values and the definition of eq. (3.5).

Calculating the stiffness matrix $\mathbf{K}$ of the system requires the definition of the additional frames $\mathcal{S}_1(s_1)$. This can be done through the definition of its associated screw $\mathbf{s}_1(s_1)$, which takes frame $\mathcal{R}_1$ into frame $\mathcal{S}_1(s_1)$. The screw $\mathbf{s}_1(s_1)$ is evaluated as

$$\mathbf{s}_1 = \begin{bmatrix} \mathbf{0}_3^T & s_1 - l - \frac{a}{2} & 0 & 0 \end{bmatrix}^T. \tag{3.32}$$

The geometric properties of the beams' cross-sections are computed from beam theory (Pilkey, 2005; Roark and Young, 1975). We know from (Paros and Weisbord, 1965) that notched beams can be modelled as Euler-Bernoulli beams when loaded in bending or tension. However, if we observe the elastostatic properties, we realize that beam theory is not accurate enough for notched beams with a high ratio w/l. The accuracy depends on the type and direction of loading. To cope with this inaccuracy, correction factors were computed in Ansys. Since $t_i(s_i)$, the thickness of the profile of the i^{th} hinge (Fig. 3.1), is a function of s_i, the coordinate along the beam neutral axis, the properties of the beam cross-section yield

$$J_i(s_i) = \beta_J \frac{1}{12} w t_i^3(s_i) \left[\frac{16}{3} - 3.36 \frac{t_i(s_i)}{w} \left(1 - \frac{t_i^4(s_i)}{12 w^4}\right)\right] \quad \text{with} \quad \beta_J = 37.2, \tag{3.33a}$$

$$I_{Zi}(s_i) = \beta_z \frac{w^3 t_i(s_i)}{12} \quad \text{with} \quad \beta_z = 0.8, \tag{3.33b}$$

$$I_{Yi}(s_i) = \frac{w t_i^3(s_i)}{12}, \quad A_i(s_i) = w t_i(s_i), \quad \alpha_Y = \alpha_Z = 6/5. \tag{3.33c}$$

where β_J and β_z are the correction factors computed with finite element analysis. Notice that $\beta_J = 37.2$ and $\beta_z = 0.8$ when $t = 250$ μm, $l = 3$ mm, and $w = 10$ mm. As there is only one flexible link matrix $\mathbf{A}$ is a 6 by 6 identity matrix. From eq. (3.26), we obtain the stiffness matrix of the system,

$$[\mathbf{K}]_{\mathcal{F}} = \begin{bmatrix} 117.61 & 0 & 0 & 0 & 0 & 0 \\ 0 & 3951.7 & 0 & 0 & 0 & 419470 \\ 0 & 0 & 674.54 & 0 & -103440 & 0 \\ 0 & 0 & 0 & 210020 & 0 & 0 \\ 0 & 0 & -103440 & 0 & 159140 & 0 \\ 0 & 419470 & 0 & 0 & 0 & 645340 \end{bmatrix}. \tag{3.34}$$

With matrix $\mathbf{K}$ and $\mathbf{M}$ at hand, the frequency matrix-squared $\mathbf{\Omega}^2$ can be computed from its definition, in eq. (3.28). By extracting the eigenvalues and eigenvectors from matrix $\mathbf{\Omega}^2$, the natural frequencies and the modal vectors of the system are found and listed in Table 3.2. Note that the modal vectors show the direction and orientation of the motion of each rigid link when excited at its natural frequency. From the modal vectors, it is apparent that the three lower frequencies correspond, respectively, to an oscillation in the sensitive axis θ_z, the torsional axis θ_x, and, finally, the bending axis θ_y. The other three frequencies, which are second order effects, are disregarded in the analysis of the results, since they are much higher than the other frequencies. Table 3.3 shows the errors in the results of the lumped-parameter model, where the accurate values of reference were computed with finite element analysis (FEA). With errors under 5%, the lumped-parameter model gives a reliable approximation of the natural frequencies of lumped compliant mechanisms.

TABLE 3.2. Modal analysis of one notched beam system

i	1	2	3	4	5	6
f_i (rad/s)	4285.6	71210	86464	190300	30713	357770
f_i (Hz)	682	11333	13761	30287	48881	56941
$\boldsymbol{\lambda}_i$	0.00 0.00 -1.00 0.00 0.01 0.00	1.00 0.00 0.00 0.00 0.00 0.00	0.00 -1.00 0.00 0.00 0.00 0.01	0.00 0.00 -1.00 0.00 0.00 0.00	0.00 0.00 0.00 1.00 0.00 0.00	0.00 1.00 0.00 0.00 0.00 0.00

TABLE 3.3. Natural frequencies

Frequency	Orientation	Lumped-parameter model	FEA	Error
λ_1	θ_Z	682 Hz	698 Hz	2.3%
λ_2	θ_X	11333 Hz	11554 Hz	1.9%
λ_3	θ_Y	13761 Hz	13238 Hz	3.9%
λ_4	θ_Z	30287 Hz	28796 Hz	4.9%

Considering that we want to use the beams as sensors, we designed them so that they are particularly sensitive to forces parallel to the sensitive axis of the beam. Hence, for a notched beam to be a robust sensor, its sensitivity along its sensitive axis needs to be as high as possible with respect to its sensitivity in other directions. Therefore, we define the ratios below, which are to be maximized, where Z is to be the sensitive axis. For the parameter values given in Table 3.1, we obtain:

$$r_{\theta_X,\theta_Z} \equiv \frac{\lambda_2}{\lambda_1} = 16.6, \quad r_{\theta_Y,\theta_Z} \equiv \frac{\lambda_3}{\lambda_1} = 20.2. \tag{3.35}$$

These results illustrate that the notched beam hinge has good off-axis stiffness. However, one flexure hinge cannot produce a translation mechanism. This can be overcome by using four of them in a parallelogram linkage, as is done in the flexible realization of the Π-joint introduced in the Chapter 2.

TABLE 3.4. Dimensions of the 2ΠΠ system

l	t	w	a	b	e	h	θ
3 mm	250 μm	20 mm	15 mm	3 mm	20 mm	6 mm	$\pi/4$

3.3 Case Study: The Compliant 2ΠΠ System

In this section we analyze the compliant 2ΠΠ mechanical structure of the accelerometer. Figures 2.8 and 3.3 show, respectively, the parameterization of the 2ΠΠ mechanism and the orientation of the frames. The compliant mechanism is made of $m = 16$ identical compliant joints numbered inside balloons, whereas the $n = 11$ rigid-link labels of the mechanism are included in squares. The largest rigid body in the middle is the proof-mass and the other 10 rigid links are intermediate rigid bodies. As we resorted to the general case of three-dimensional beam deflection theory, we consider the six degrees of freedoms of each rigid link. Thus, the compliant accelerometer is modelled as a mass-spring system of 66 degrees of freedom. The dimensions of the mechanism layout are recorded in Table 3.4. Here, we see that two rules apply in the numbering of the rigid links. First, the frames $\mathcal{F}$ and $\mathcal{R}_1$ must be fixed at the centre of mass of the proof-mass in order to ease the analysis of the modal vectors. Second, the rigid links of the parallelogram are numbered successively. Here, frames $\mathcal{F}$ and $\mathcal{R}_j$, $j = 1, ..., n$, $n = 11$, are defined as displayed in Fig. 3.3, where the X axes are oriented in the direction of the sensitive axis of the accelerometer.

3.3.1 Kinetic Energy.

Frames $\mathcal{R}_j$, $j = 1, ..., n$, $n = 3$, are located so that screws r_j , $j = 1, \ldots, n$, $n = 3$, take the values

$$\mathbf{r}_1 = \mathbf{0}_6^T,$$

$$\mathbf{r}_2 = \begin{bmatrix} \mathbf{0}_3^T & -l - (ac\theta + e)/2 & (as\theta + w - h)/2 & 0 \end{bmatrix}^T,$$

$$\mathbf{r}_3 = \begin{bmatrix} \mathbf{0}_3^T & -l - (ac\theta + e)/2 & (as\theta - w + h)/2 & 0 \end{bmatrix}^T,$$

$$\mathbf{r}_4 = \begin{bmatrix} \mathbf{0}_3^T & -2l - ac\theta - (e + b)/2 & as\theta & 0 \end{bmatrix}^T,$$

$$\mathbf{r}_5 = \begin{bmatrix} \mathbf{0}_3^T & -3l - b - (3ac\theta + e)/2 & (as\theta + w - h)/2 & 0 \end{bmatrix}^T,$$

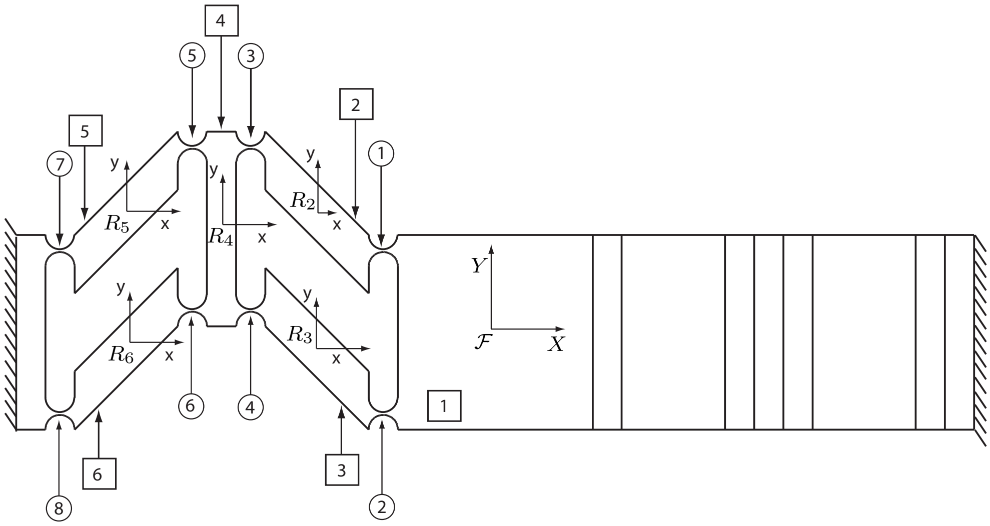

(A)

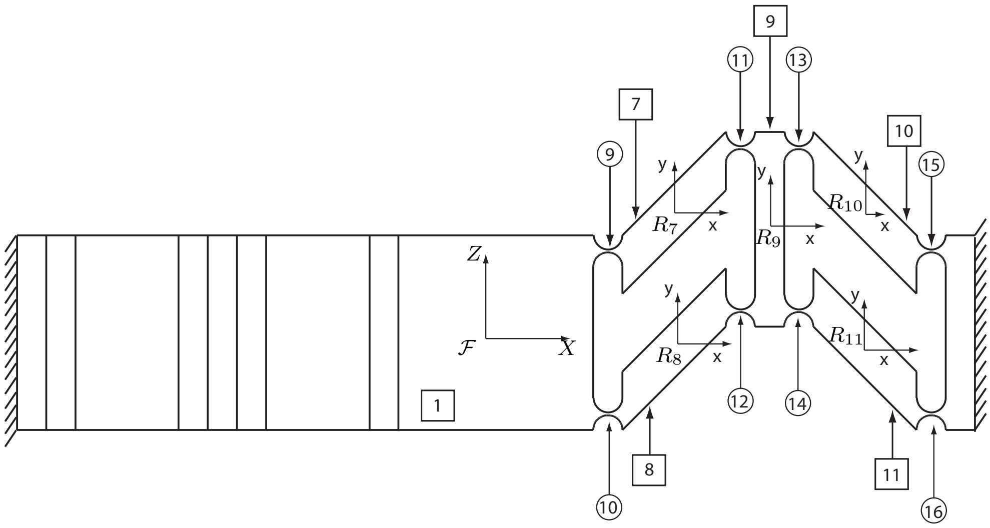

(B)

FIGURE 3.3. Uniaxial accelerometer: (a) front view; and (b) bottom view

$$\mathbf{r}_6 = \begin{bmatrix} \mathbf{0}_3^T & -3l - b - (3ac\theta + e)/2 & (as\theta - w + h)/2 & 0 \end{bmatrix}^T,$$
$$\mathbf{r}_7 = \begin{bmatrix} \pi/2 & 0 & 0 & l + (ac\theta + e)/2 & 0 & (as\theta + w - h)/2 \end{bmatrix}^T,$$
$$\mathbf{r}_8 = \begin{bmatrix} \pi/2 & 0 & 0 & l + (ac\theta + e)/2 & 0 & (as\theta - w + h)/2 \end{bmatrix}^T,$$
$$\mathbf{r}_9 = \begin{bmatrix} \pi/2 & 0 & 0 & 2l + ac\theta + (e + b)/2 & 0 & as\theta \end{bmatrix}^T,$$
$$\mathbf{r}_{10} = \begin{bmatrix} \pi/2 & 0 & 0 & 3l + b + (3ac\theta + e)/2 & (as\theta + w - h)/2 & 0 \end{bmatrix}^T,$$
$$\mathbf{r}_{11} = \begin{bmatrix} \pi/2 & 0 & 0 & -3l - b - (3ac\theta + e)/2 & (as\theta - w + h)/2 & 0 \end{bmatrix}^T,$$

where

$$c\theta = \cos\theta \qquad s\theta = \sin\theta \tag{3.36}$$

The mass properties of the rigid links yield

$$m_1 = \rho e w^2, \quad m_4 = m_9 = \rho b w^2$$

$$m_k = \rho a h w c\theta, \quad k = 2, 3, 5, 6, 7, 8, 10, 11$$

$$[\mathbf{I}_1]_{\mathcal{R}_1} = [\mathbf{I}_1]_{\mathcal{F}} = \begin{bmatrix} 2w^2 & 0 & 0 \\ 0 & e^2 + w^2 & 0 \\ 0 & 0 & e^2 + w^2 \end{bmatrix} \frac{\rho e w^2}{12}$$

$$[\mathbf{I}_i]_{\mathcal{R}_i} = \begin{bmatrix} (as\theta)^2 + h^2 + w^2 & -a^2 c\theta s\theta & 0 \\ -a^2 c\theta s\theta & (ac\theta)^2 + w^2 & 0 \\ 0 & 0 & (ac\theta)^2 + (as\theta)^2 + a^2 \end{bmatrix} \frac{\rho h w^2 a c\theta}{12}, \quad i = 2, 3, 10, 11$$

$$[\mathbf{I}_i]_{\mathcal{R}_i} = \begin{bmatrix} (as\theta)^2 + h^2 + w^2 & 0 & -a^2 c\theta s\theta \\ 0 & (ac\theta)^2 + (as\theta)^2 + a^2 & 0 \\ -a^2 c\theta s\theta & 0 & (ac\theta)^2 + w^2 \end{bmatrix} \frac{\rho h w^2 a c\theta}{12}, \quad i = 5, 6, 7, 8$$

$$[\mathbf{I}_4]_{\mathcal{R}_4} = [\mathbf{I}_9]_{\mathcal{R}_9} = \begin{bmatrix} 2w^2 & 0 & 0 \\ 0 & b^2 + w^2 & 0 \\ 0 & 0 & b^2 + w^2 \end{bmatrix} \frac{\rho b w^2}{12},$$

The mass matrix is evaluated directly from these numerical values and the definitions of eq. (3.11).

3.3.2 Potential Energy. Upon defining the lengths $L = e + 2b + 8l + 4a\cos\theta$, screws s_i, $i = 1, \ldots, m$, $m = 16$, are evaluated as

$$[\mathbf{s}_1]_{\mathcal{R}_1} = \begin{bmatrix} 0 & \pi & 0 & -e/2 - s_1 & (w - t - l)/2 & 0 \end{bmatrix}^T,$$

$$
\begin{aligned}
[\mathbf{s}_2]_{\mathcal{R}_1} &= \begin{bmatrix}0 & \pi & 0 & -e/2 - s_2 & (-w+t+l)/2 & 0\end{bmatrix}^T, \\
[\mathbf{s}_3]_{\mathcal{R}_2} &= \begin{bmatrix}0 & \pi & 0 & -ac\theta/2 - s_3 & (as\theta+h-l-t)/2 & 0\end{bmatrix}^T, \\
[\mathbf{s}_4]_{\mathcal{R}_3} &= \begin{bmatrix}0 & \pi & 0 & -ac\theta/2 - s_4 & (as\theta-h+l+t)/2 & 0\end{bmatrix}^T, \\
[\mathbf{s}_5]_{\mathcal{R}_4} &= \begin{bmatrix}0 & \pi & 0 & -b/2 - s_5 & (w-t-l)/2 & 0\end{bmatrix}^T, \\
[\mathbf{s}_6]_{\mathcal{R}_4} &= \begin{bmatrix}0 & \pi & 0 & -b/2 - s_6 & (-w+t+l)/2 & 0\end{bmatrix}^T, \\
[\mathbf{s}_7]_{\mathcal{F}} &= \begin{bmatrix}\mathbf{0}_3^T & -L/2 + s_7, (w-t-l)/2 & 0\end{bmatrix}^T, \\
[\mathbf{s}_8]_{\mathcal{F}} &= \begin{bmatrix}\mathbf{0}_3^T & -L/2 + s_8, (-w+t+l)/2 & 0\end{bmatrix}^T, \\
[\mathbf{s}_9]_{\mathcal{R}_1} &= \begin{bmatrix}\pi/2 & 0 & 0 & e/2 + s_9 & 0 & (w-t-l)/2\end{bmatrix}^T, \\
[\mathbf{s}_{10}]_{\mathcal{R}_1} &= \begin{bmatrix}\pi/2 & 0 & 0 & e/2 + s_{10} & 0 & (-w+t+l)/2\end{bmatrix}^T, \\
[\mathbf{s}_{11}]_{\mathcal{R}_7} &= \begin{bmatrix}\mathbf{0}_3^T & ac\theta/2 + s_{11} & (as\theta+h-l-t)/2 & 0\end{bmatrix}^T, \\
[\mathbf{s}_{12}]_{\mathcal{R}_8} &= \begin{bmatrix}\mathbf{0}_3^T & ac\theta/2 + s_{12} & (as\theta-h+l+t)/2 & 0\end{bmatrix}^T, \\
[\mathbf{s}_{13}]_{\mathcal{R}_9} &= \begin{bmatrix}\mathbf{0}_3^T & b/2 + s_{13} & (w-t-l)/2 & 0\end{bmatrix}^T, \\
[\mathbf{s}_{14}]_{\mathcal{R}_9} &= \begin{bmatrix}\mathbf{0}_3^T & b/2 + s_{14} & (-w+t+l)/2 & 0\end{bmatrix}^T, \\
[\mathbf{s}_{15}]_{\mathcal{F}} &= \begin{bmatrix}0 & \sqrt{2}\pi/2 & \sqrt{2}\pi/2 & L/2 - s_{15} & 0 & (w-t-l)/2\end{bmatrix}^T, \\
[\mathbf{s}_{16}]_{\mathcal{F}} &= \begin{bmatrix}0 & \sqrt{2}\pi/2 & \sqrt{2}\pi/2 & L/2 - s_{16} & 0 & (-w+t+l)/2\end{bmatrix}^T.
\end{aligned}
$$

As the notched beams have the same layout as the revolute joint studied in section 3.2, their cross-section have the properties given in eq.(3.33). From the dimensions listed in Table 3.4, we can compute the stiffness matrix $\mathbf{K}$ of the system.

3.3.3 Mathematical Model. We derived the natural frequencies of the system from the eigenvalues of matrix $\mathbf{\Omega}^2$. The four lowest frequencies and their corresponding normalized modal vectors are listed in Table 3.5. As expected, the first natural frequency, $\lambda_1 = 290$ Hz, corresponds to an oscillation of the proof-mass in the X direction. The second and third natural frequencies, $\lambda_2 = 1013$ Hz and $\lambda_3 = 1066$ Hz, are almost equal due to the isotropic stiffness, while the gap between the two frequencies results in the axis drift. The axis drift also causes the proof-mass to move out of the sensitive axis when subjected to accelerations parallel to the sensitive axis. The parasitic motion generated by the axis drift, which is shown by the modal vector $\boldsymbol{\lambda}_{1,1}$, is a combining parasitic rotation around the X, Y and Z axes. To analyze the off-axis sensitivity, we can once more compute the ratios of sensitivity, yielding

$$r_{\theta_Z,X} \equiv \frac{\lambda_2}{\lambda_1} = 3.49 \ , \quad r_{\theta_Y,X} \equiv \frac{\lambda_3}{\lambda_1} = 3.67 \ , \quad r_{\theta_X,X} \equiv \frac{\lambda_4}{\lambda_1} = 7.33 \tag{3.37}$$

The loss of off-axis stiffness compared with the notched beam of Section 3.2 comes from the serial configuration of the accelerometer, and from the asymmetric configuration of the ΠΠ-legs. Undoubtedly, as Moon et al. (2002) point out, a symmetric configuration of compliant joints greatly improves the ratio of off-axis stiffness to sensitive-axis stiffness; furthermore it eliminates a major part of the axis drift, improving the precision in the measurement of displacement of the proof-mass. As long as we want to have at least one order of magnitude between λ_2 and λ_1, a new topology for the simplicial uniaxial accelerometer is required.

3.4 Alternative Layout

There are two ways to improve the ratio of the off-axis stiffness to sensitive-axis stiffness and the axis-drift of the compliant realization of the SUA. The first consists of adding extra ΠΠ-legs to each side of the proof-mass. This solution requires more space, thereby penalizing the compactness of the accelerometer. The second and best way, consists in merging the two intermediate rigid links connecting the two Π-joints of the ΠΠ-legs with the proof-mass and in fixing each Π-joint to the frame of the accelerometer. The new layout of the mechanism, as shown in Fig. 3.4a, is the most compact form of the SUA because it is the layout with the lowest number of rigid and flexible links. Moreover, the Π-joints of the new layout is made of uniform cross-section beams, which are more compact than the notched beams Π-joints used in the original layout. The new layout is not only the most compact form of the SUA, but it also offers an excellent ratio of the off-axis stiffness to sensitive-axis stiffness. By

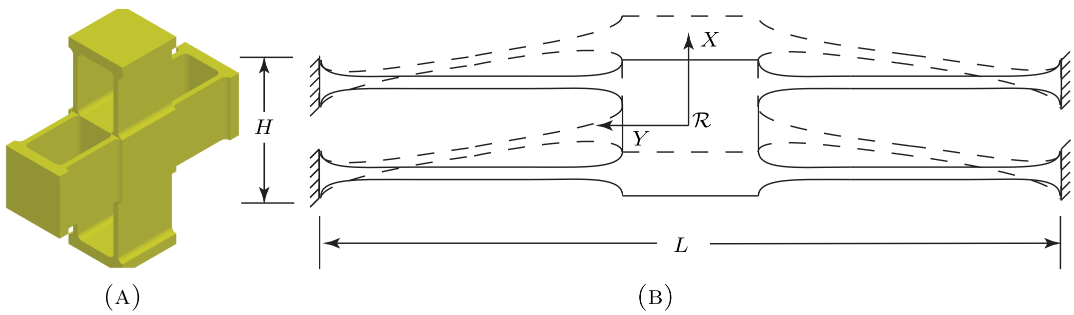

FIGURE 3.4. New layout: (a) CAD model; and (b) deformation along the sensitive axis

using straight flexible beams rather than circular hinges to create the approximation of Π-joints we eliminate all intermediate rigid links likely to bring parasitic inertia forces by acting as seismic masses. Figure 3.4b illustrates the behaviour of the new layout mechanism subjected to acceleration along the sensitive-axis direction. The mechanism works on the principle of large-displacement compliant joint developed by Moon et al. (2002). The dimensions of the mechanism studied in this work are recorded in Table 3.6.

Frames $\mathcal{F}$ and $\mathcal{R}_1$ are defined as displayed in Fig. 3.5, with their X axes along the direction of the sensitive axis. Moreover, the origins O and R_1 of these two frames are located at the proof-mass centroid. Since frames $\mathcal{F}$ and $\mathcal{R}_1$ are coincident, we have

$$\mathbf{R}_1 = \mathbf{1}_{6\times 6}. \tag{3.38}$$

The mass matrix $\mathbf{M}$ of the mechanism is the mass matrix of the proof mass as defined in eq. (3.5). The beam cross-section remains constant in all the compliant links, and hence,

$$J_i = \frac{1}{12} w t^3 \left[\frac{16}{3} - 3.36 \frac{t}{w}\left(1 - \frac{t^4}{12 w^4}\right)\right], \tag{3.39a}$$

$$I_{Yi} = \frac{w t^3}{12}, \quad I_{Zi} = \frac{w^3 t}{12}, \quad A_i = wt, \quad \alpha_Y = \alpha_Z = 6/5. \tag{3.39b}$$

The screws $s_i, i = 1, ..., m$, $m = 8$, are evaluated as

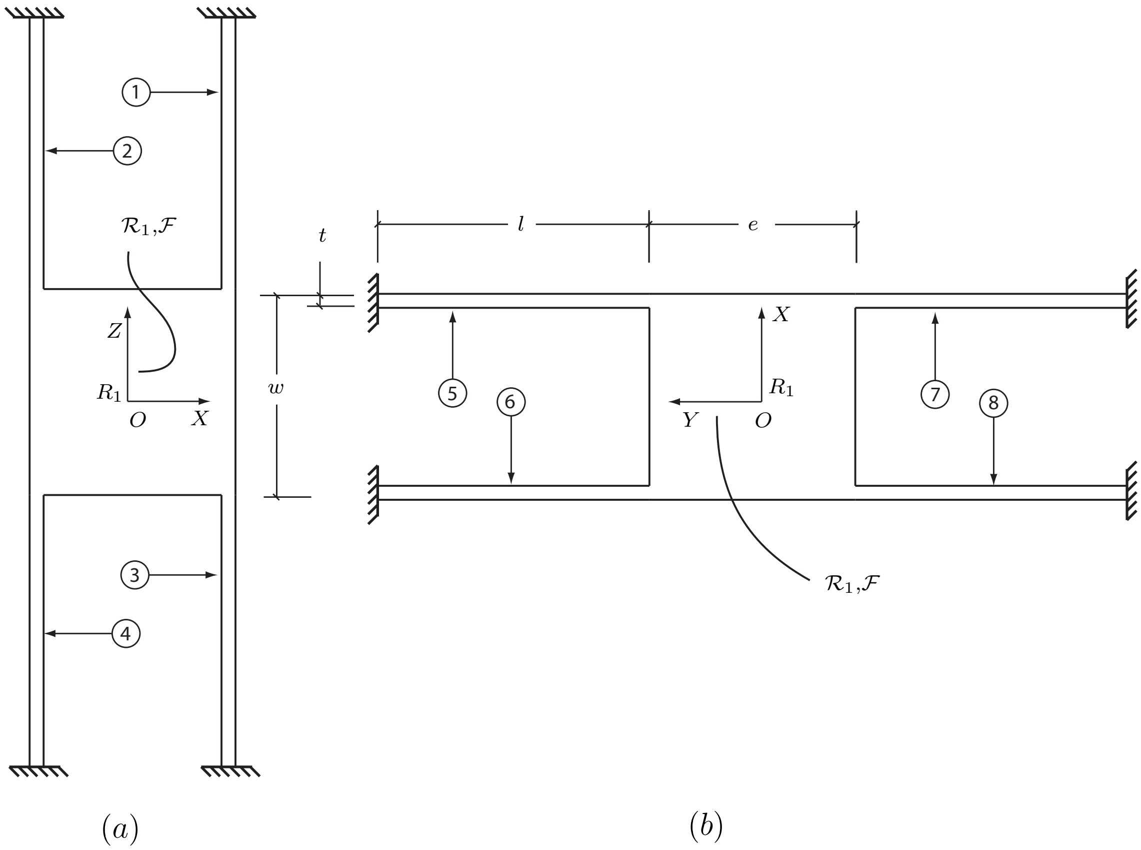

FIGURE 3.5. New layout of the uniaxial accelerometer: (a) left view; and (b) top view

$$
\begin{aligned}
[\mathbf{s}_1]_{\mathcal{F}} &= \begin{bmatrix}0 & \pi/2 & 0 & e/2 & 0 & w/2+l-s_1\end{bmatrix}^T,\\
[\mathbf{s}_2]_{\mathcal{F}} &= \begin{bmatrix}0 & \pi/2 & 0 & -e/2 & 0 & w/2+l-s_2\end{bmatrix}^T,\\
[\mathbf{s}_3]_{\mathcal{F}} &= \begin{bmatrix}0 & -\pi/2 & 0 & e/2 & 0 & -w/2-l+s_3\end{bmatrix}^T,\\
[\mathbf{s}_4]_{\mathcal{F}} &= \begin{bmatrix}0 & -\pi/2 & 0 & e/2 & 0 & -w/2-l+s_4\end{bmatrix}^T,\\
[\mathbf{s}_5]_{\mathcal{F}} &= \begin{bmatrix}0 & 0 & -\pi/2 & e/2 & w/2+l-s_5 & 0\end{bmatrix}^T,\\
[\mathbf{s}_6]_{\mathcal{F}} &= \begin{bmatrix}0 & 0 & -\pi/2 & -e/2 & w/2+l-s_6 & 0\end{bmatrix}^T,\\
[\mathbf{s}_7]_{\mathcal{F}} &= \begin{bmatrix}0 & 0 & \pi/2 & e/2 & -w/2-l+s_7 & 0\end{bmatrix}^T,\\
[\mathbf{s}_8]_{\mathcal{F}} &= \begin{bmatrix}0 & 0 & \pi/2 & -e/2 & -w/2-l+s_8 & 0\end{bmatrix}^T.
\end{aligned}
$$

Once again, we find the natural frequencies of the system from the eigenvalues of matrix $\mathbf{\Omega}^2$ The four lowest frequencies and their corresponding modal vectors are listed in Table 3.7. The first natural frequency, $\lambda_1 = 490.6$ Hz, remains in the sensitive axis, but the mechanism uses the second order deformation of the flexible beam to allow the translation of the proof-mass. The plane normal to the sensitive axis is isotropically rigid, in that the second and third frequencies are equal. Moreover, the mechanism is not subjected to axis drift since the components of vector $\boldsymbol{\lambda}_1$ are at zero, with the exception of the component corresponding to translation along the X direction. The sensitivity ratios of the new layout,

$$r_{\theta_Z,X} \equiv \frac{\lambda_2}{\lambda_1} = 7.98, \quad r_{\theta_Y,X} \equiv \frac{\lambda_3}{\lambda_1} = 8.05 \tag{3.40}$$

We notice here that the sensitivity ratio reveal almost one order of magnitude of difference between λ_2 and λ_1. In addition, the sensitive off-axis plane is isotropic, since $r_{\theta_Y,X} \approx r_{\theta_Z,X}$. The new layout is less sensitive than its original 2ΠΠ counterpart, because the former uses the second order deformation of the flexible beams to allow the translation of the proof-mass. However, λ_1 does not exceed the maximum natural frequency, 1800 Hz, of low-frequency accelerometers (see Chapter 1). Moreover, it is possible to improve the accelerometer properties by optimizing the new layout.

TABLE 3.5. Modal frequencies and modal vectors of the compliant 2ΠΠ mechanism

i	1	2	3	4	i	1	2	3	4
f_i (Hz)	290	1013	1066	2128	f_i (Hz)	290	1013	1066	2128
$\boldsymbol{\lambda}_{i,1}$	0.301	−0.032	0.076	0.931	$\boldsymbol{\lambda}_{i,7}$	0.000	−0.524	−0.423	−0.982
	0.197	−0.697	0.726	0.244		0.000	0.121	0.175	0.118
	−0.181	0.716	0.678	0.212		−1.000	−0.843	0.889	0.148
	−0.915	0.000	0.000	0.000		0.000	0.000	0.000	0.000
	0.000	0.000	−0.063	0.000		0.000	0.000	0.000	0.000
	0.000	0.000	−0.068	0.000		0.000	0.000	0.000	0.000
$\boldsymbol{\lambda}_{i,2}$	0.000	−0.489	0.505	0.980	$\boldsymbol{\lambda}_{i,8}$	0.000	−0.745	−0.488	−0.920
	0.000	−0.107	0.201	0.114		0.000	0.115	0.199	0.320
	−1.000	−0.866	−0.839	−0.160		−1.000	−0.657	0.850	0.228
	0.000	0.000	0.000	0.000		0.000	0.000	0.000	0.000
	0.000	0.000	0.000	0.000		0.000	0.000	0.000	0.000
	0.000	0.000	0.000	0.000		0.000	0.000	0.000	0.000
$\boldsymbol{\lambda}_{i,3}$	0.000	−0.720	0.601	0.924	$\boldsymbol{\lambda}_{i,9}$	0.199	−0.898	0.156	−0.977
	0.000	−0.104	0.224	0.296		−0.143	0.375	0.794	0.131
	−1.000	−0.686	−0.767	−0.241		−0.105	0.228	−0.581	−0.167
	0.000	0.000	0.000	0.000		−0.593	0.000	0.000	0.000
	0.000	0.000	0.000	0.000		−0.760	0.000	−0.060	0.000
	0.000	0.000	0.000	0.000		0.000	0.000	0.000	0.000
$\boldsymbol{\lambda}_{i,4}$	0.187	−0.904	0.000	0.978	$\boldsymbol{\lambda}_{i,10}$	0.000	0.230	0.613	−0.999
	0.157	−0.344	0.840	0.124		0.000	0.162	0.094	0.000
	−0.093	0.252	0.535	0.169		1.000	−0.960	0.784	0.051
	−0.594	0.000	0.000	0.000		0.000	0.000	0.000	0.000
	0.761	0.000	−0.059	0.000		0.000	0.000	0.000	0.000
	0.000	0.000	0.000	0.000		0.000	0.000	0.000	0.000
$\boldsymbol{\lambda}_{i,5}$	0.000	0.133	−0.622	0.999	$\boldsymbol{\lambda}_{i,11}$	0.000	0.706	0.517	−0.950
	0.000	−0.135	0.100	0.000		0.000	0.111	0.084	0.000
	1.000	−0.982	−0.776	0.000		1.000	−0.699	0.852	0.308
	0.000	0.000	0.000	0.000		0.000	0.000	0.000	0.000
	0.000	0.000	0.000	0.000		0.000	0.000	0.000	0.000
	0.000	0.000	0.000	0.000		0.000	0.000	0.000	0.000
$\boldsymbol{\lambda}_{i,6}$	0.000	0.643	−0.551	0.951					
	0.000	−0.100	0.090	0.000					
	1.000	−0.759	−0.829	−0.306					
	0.000	0.000	0.000	0.000					
	0.000	0.000	0.000	0.000					
	0.000	0.000	0.000	0.000					

TABLE 3.6. Dimensions of the new layout

l	t	w	e
10 mm	250 μm	5 mm	5 mm

TABLE 3.7. Modal analysis of the new layout

i	1	2	3	4
f_i (Hz)	1679	13407	13511	13820
$\boldsymbol{\lambda}_i$	0.00	0.14	0.17	0.23
	0.00	0.82	0.11	0.43
	0.00	0.23	0.85	0.34
	1.00	0.01	0.04	0.45
	0.00	0.03	0.01	0.32
	0.00	0.02	0.03	0.45

CHAPTER 4

Shape Optimization of a Corner-filleted Hinge

In Chapter 3 the compliant devices were designed based on the stiffness properties of its flexible elements. However, kinematic synthesis does not consider all the characteristics of compliant mechanisms. As stated by Moon et al. (2002) and De Bona and Munteanu (2005), one of the main drawbacks of a compliant hinge is the high stress concentration leading to low fatigue strength. The stress concentration depends on the stress flow which is controlled by the change of curvature in the beam. Accordingly, designers of a compliant mechanism must take into account not only the stiffness requirement, but also the strength requirement. For this reason, we choose to optimize the shape of the flexible-link profile in terms of the stress-concentration factor.

Straight flexible beams used for compliant mechanisms are integrated within a monolithic structure by adding a radius at the interface between the beam and the rigid link. Thus, the resulting flexible beam is said to be a corner-filleted hinge. However, the circular profile of the fillets, which is the most common shaped found in the literature (Stuart et al., 1997; Yingfei and Zhaoying, 2002), is not optimal with respect to stress concentration because circular fillets give rise to G^2-discontinuities, i.e. discontinuities in the curvature of a geometric curve. We know from Williams

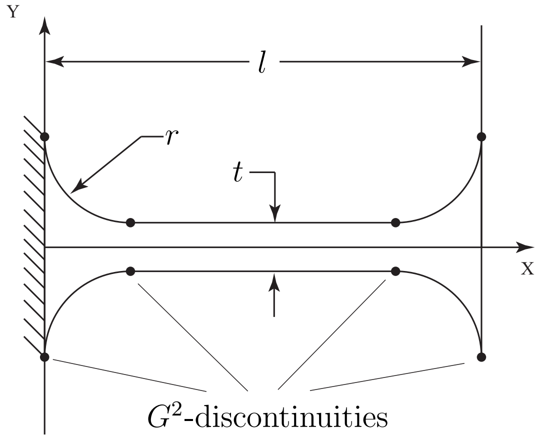

FIGURE 4.1. Corner filleted hinge

(1952), Dunn et al. (1997), and Pedersen (2007) that curvature discontinuities in the structure profile generate stress concentrations. The stress concentration resulting from the discontinuities of the corner filleted hinge profile depicted in Fig 4.1 can drastically accelerate fatigue failure and reduce the life of the compliant mechanism. What is proposed in this work is to optimize the fillet profile of the flexible beam by designing their shape with Lamé curves. By controlling the curvature of the fillet, the stress flow might be smoothed, to decrease the stress values.

De Bona and Munteanu (2005) proposed an optimum compliant hinge using a cubic-spline curve to find the best profile which will maximize the flexibility of a compliant revolute joint (Fig. 2.1a). In this thesis, we choose Lamé curves as opposed to other families of curves, e.g. splines, because of their simplicity. The true optimum shape can be obtained by resorting to calculus of variations, whereby the dimension of the design space is infinite. Lamé curves are defined, on the contrary, on a two-dimensional space, as a Lamé curve is defined by two independent parameters, as explained below.

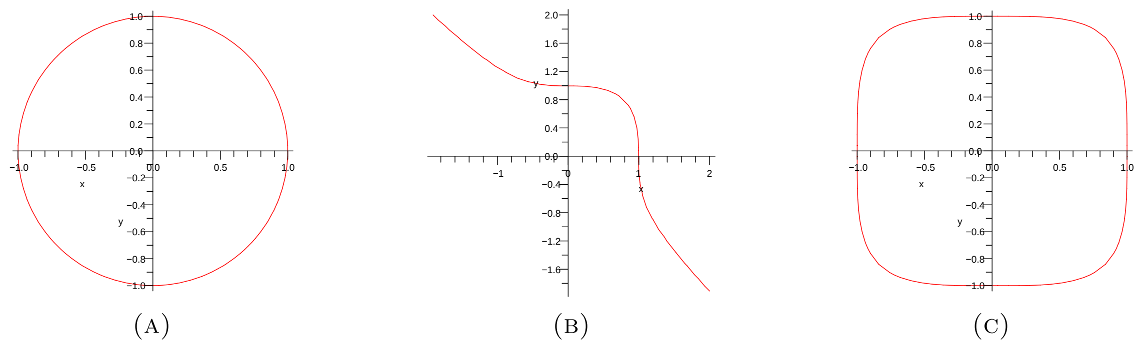

FIGURE 4.2. Lamé curves for: (a) $\eta = 2$; (b) $\eta = 3$; and (c) $\eta = 4$

4.1 Lamé Curves

Lamé curves are η-order curves defined by the equation

$$\left(\frac{x}{b_x}\right)^\eta + \left(\frac{y}{b_y}\right)^\eta = 1 \tag{4.1}$$

where η can be any rational number, while b_x and b_y correspond to the intersections of the curve with x and y axes. There are nine different types of Lamé curves based on the form of the exponent η (Loria, 1902). For our study, we resort to $\eta > 2$. From eq. (4.1), it is apparent that Lamé curves are analytic everywhere and, as shown in Fig. 4.2, even-integer-powered curves are closed and doubly symmetric. For $\eta = 2$, the curve results in a circle and, as η tends to infinity, the curve approaches a square. In the case of odd-integer-powered Lamé curves, as depicted in Fig. 4.2b, they are open and extend infinitely toward an asymptote crossing the second and the four quadrants and passing through the origin. Fractional-powered Lamé curves are also open and analytic in the first quadrant, but in the other quadrants, eq. (4.1) leads to complex numbers.

In order to obtain a closed curve for any rational power η, eq. (4.1) is modified to read

$$\left|\frac{x}{b_x}\right|^\eta + \left|\frac{y}{b_y}\right|^\eta = 1 \tag{4.2}$$

Figure 4.3 shows the curves obtained using eq. (4.2), for $\eta = 2,\ 3.5,\ 5,\ 8$, and 30. Absolute-value bars are essential for all the rational-powered curves, but can be

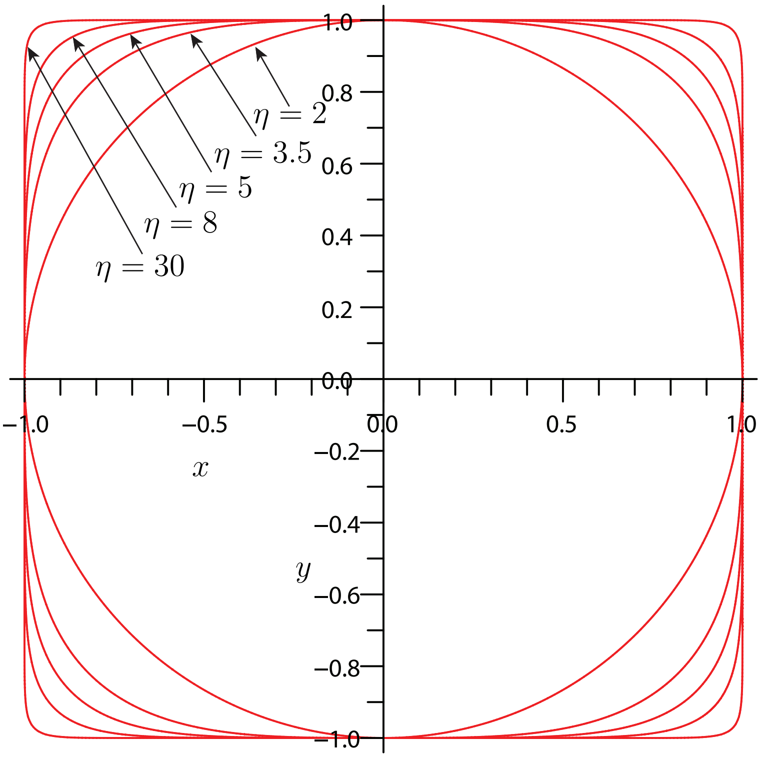

FIGURE 4.3. Lamé curves of eq. (4.2)

deleted for even-integer-powered curves. Absolute values, however, introduce discontinuities in the curvature because the absolute value function is not differentiable at the origin.

As the curves shown in Fig. 4.3 have double symmetry, it is sufficient to study only the first quadrant of the curves for the generation of the fillets. Therefore, the curves that generate the fillets take the form:

$$f(x, y) = \left(\frac{x}{b_x}\right)^{\eta} + \left(\frac{y}{b_y}\right)^{\eta} - 1 = 0; \quad 2 < \eta \in \mathbb{Q}, x, y \in \mathbb{R}^{+} \tag{4.3}$$

where $\mathbb{Q}$ is the set of rational numbers and b_x and b_y are scaling parameters. Apparently, Lamé curves have two independent parameters, the ratio b_y/b_x and η.

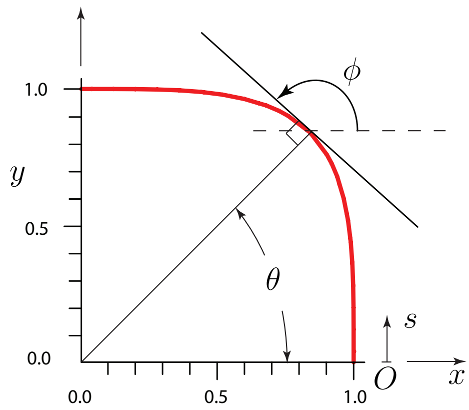

FIGURE 4.4. Lamé curves polar coordinate for $\eta = 4$

4.1.1 Parameterization of Lamé Curves. With regard to eq. (4.3), the x and y coordinates can be defined explicitly in terms of θ as:

$$x(\theta) = \frac{1}{(1 + \tan\theta^{\eta})^{\frac{1}{\eta}}}, \quad y(\theta) = \frac{\tan\theta}{(1 + \tan\theta^{\eta})^{\frac{1}{\eta}}} \tag{4.4}$$

where the angle $\theta \in [0, \pi/2]$ is the polar coordinate of one point of the curve, measured with respect to the x-coordinate axis, and is defined positive counterclockwise. To generate the shape of the fillets, affine transformations are used to scale the coordinate x_1 and y_1 by means of parameters b_x and b_y, namely,

$$x_1(\theta) = \frac{b_x}{(1 + \tan\theta^{\eta})^{1/\eta}}, \quad y_1(\theta) = \frac{b_y \tan\theta}{(1 + \tan\theta^{\eta})^{1/\eta}} \tag{4.5}$$

If $b_x = b_y = b$, the Lamé curve has a super circular layout; otherwise $(b_x \neq b_y)$, the Lamé curve has a super elliptical layout. Thus, Lamé curves can create two types of fillet: the supercircular fillet and the superelliptical fillet.

4.1.2 Curvature of Lamé Curves. The advantage of this family of curves is that for $\eta > 2$ their curvature vanishes at the intersections with the coordinate axes. The curvature $\kappa(s)$ is defined as

$$\kappa(s) \equiv \frac{d\phi}{ds} \tag{4.6}$$

where ϕ is the angle made by the tangent with a fixed line and s is the curve length, as shown in Fig. 4.4. From its definition, curvature has units of inverse length. If the Lamé curve is given by the parametric form of eq. (4.4), then the curvature $\kappa(\theta)$ takes the form

$$\kappa(\theta) = \frac{x'(\theta)y''(\theta) - y'(\theta)x''(\theta)}{(x'(\theta)^2 + y'(\theta)^2)^{3/2}} \tag{4.7}$$

Notice that for $\eta > 2$, $\kappa(\theta)$ becomes undefined at $\theta = 0$ and $\pi/2$, but the continuity of the curvature at points $(1, 0)$ and $(0, 1)$ can be shown to be preserved by computing the limit of $\kappa(\theta)$ as θ approaches 0 or $\pi/2$.

$$\lim_{\substack{\theta\to 0\\ \eta>2}} \kappa(\theta) = \lim_{\substack{\theta\to \pi/2\\ \eta>2}} \kappa(\theta) = 0 \tag{4.8}$$

The curvature can be expressed in a more robust form, namely, implicit (Gray, 1993):

$$\kappa(x, y) = \frac{2f_{xy}f_x f_y - f_{xx}f_y^2 - f_{yy}f_x^2}{(f_x^2 + f_y^2)^{3/2}} \tag{4.9}$$

where f_x and f_{xx} are the first-and second-order partial derivatives of $f(x, y) = 0$ with respect to x, f_y and f_{yy} being defined likewise, and f_{xy} is the mixed second-order partial derivative of $f(x, y) = 0$. For the curve $f(x, y)$ of eq.(4.3) the curvature takes the form (Khan, 2007)

$$\kappa(x, y) = \frac{(\eta - 1)(xy)^{\eta-2}(x^\eta + y^\eta)}{(x^{2\eta-2} + y^{2\eta-2})^{3/2}} \tag{4.10}$$

whence, apparently the curvature of rational-powered Lamé curves vanishes at the intersection with the coordinate axes.

The three different profiles of the flexible beam studied in this thesis, are the profiles made of circular fillets, supercircular fillets, and superelliptical fillets, as represented, respectively, in Figs. 4.5a, c, and e. Their corresponding curvature distributions in terms of s are illustrated in Figs. 4.5b, d, and f. Each profile has singular points A and B at the blending points of the curve and the straight line. For the case of the circular fillet, the curvature attains unbounded values at the singular points A,

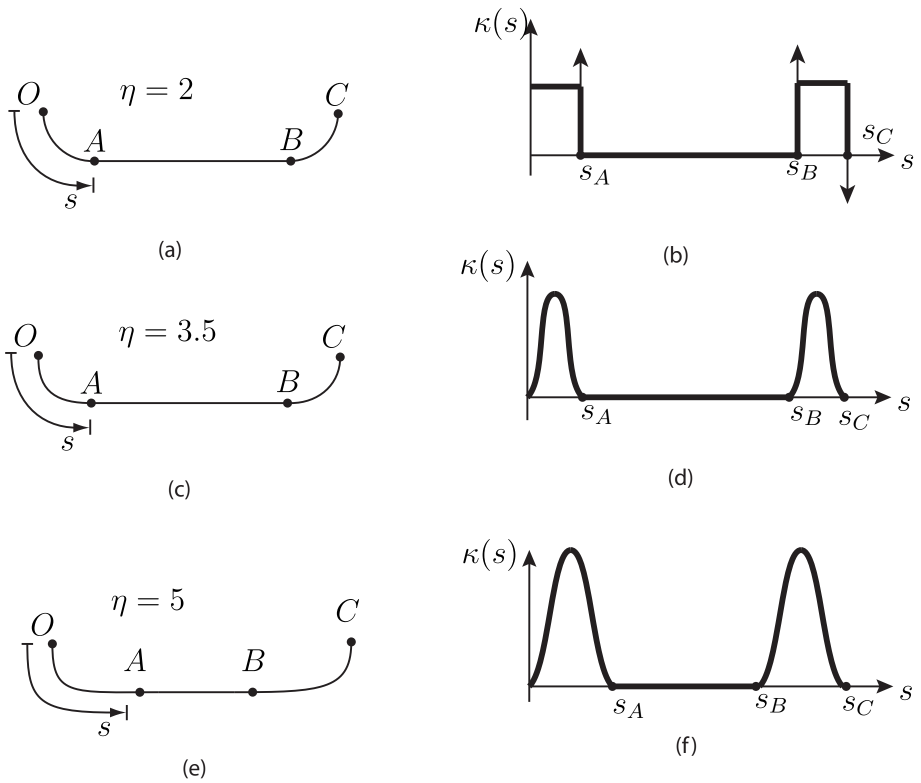

FIGURE 4.5. Flexible beam profiles and their corresponding curvature distributions: (a) (b) circular fillets; (c) (d) supercircular fillets; and (e) (f) superelliptical fillets

B and C. The curvature at the singular points is thus indicated with an arrow, to indicate the presence of a Dirac function. On the other hand, the curvature of the supercircular and the superelliptical profiles depicted in Figs. 4.5d and f are continuous everywhere, which shows that their corresponding flexible beams are G^2-continuous everywhere.

4.2 Basic Problem

In this work, we consider the supercircular and the superelliptical fillets of Figs. 4.6a and b, the former becoming a circular fillet for $\eta = 2$. However, a circular fillet is not a good profile because it is G^2-discontinuous. Here, our goal is to search for the power ($\eta > 2$) of the Lamé curve that minimizes the stress concentration without compromising the compliance of the joint.

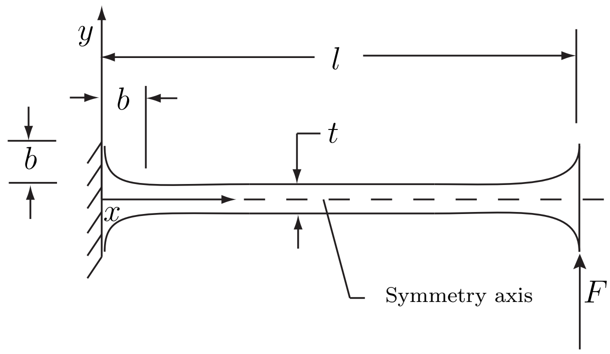

(A)

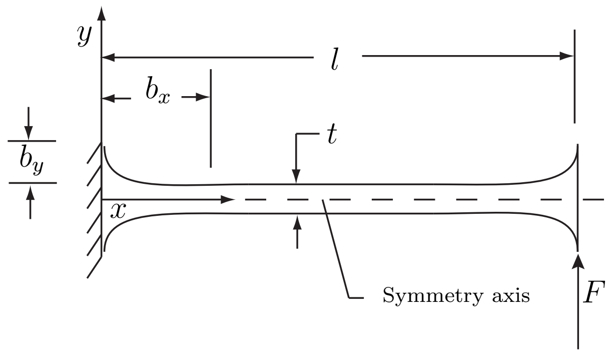

(B)

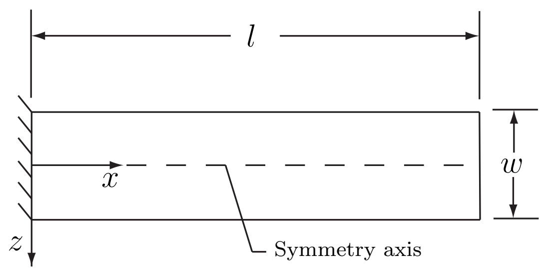

(C)

FIGURE 4.6. Geometry of a Lamé-filleted hinge: (a) supercircular filleted hinge; (b) superelliptical filleted hinge; (c) top view of both hinges

4.3 Structural Optimization Procedure

4.3.1 General Scheme. Flexibility along the sensitive axis is the main requirement that has to be fulfilled when designing a flexural beam. Therefore, the reduction of stress concentration must not decrease the flexibility of the beam along the sensitive axis. It follows that the design problem can be solved by referring to

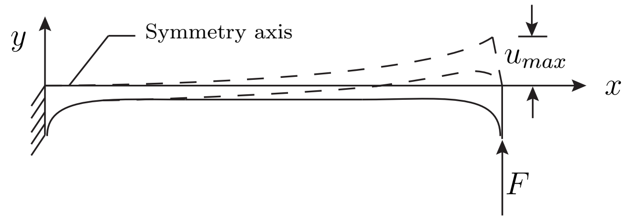

(A)

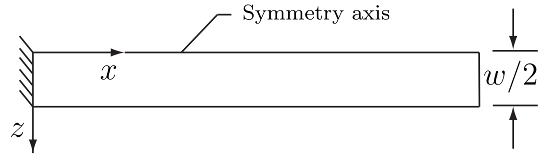

(B)

FIGURE 4.7. Structural model: (a) front view, (b) top view

a classical optimization procedure, where the minimum stress concentration is the objective function with a constraint on the joint flexibility. Objective function and constraint must be computed by a Finite Element (FE) solver because closed-form solutions of stresses are not possible for arbitrary shapes. Moreover, only FE analysis with a fine mesh can determine local stress peaks generated by G^2-discontinuities. A procedure was set-up for the automatic generation of the FE mesh at each optimization step according to the values of the design variables provided by the optimization algorithm.

By exploiting the layout symmetry, we can simplify the structural model of the hinge to only a quarter of the original structure. Figures 4.6a, b, and c show the axis of symmetry for the analysis. A symmetry condition applies to problems in which the geometry, loading, and boundary conditions are symmetric about an axis, while, an anti-symmetry condition applies when only the geometry is symmetric with respect to an axis (Moaveni, 2003). In the anti-symmetry case, the loading and the boundary conditions are not symmetrically spread on each side of the anti-symmetric axis. Figure 4.7 shows the model used for the structural analysis and the planes subject to the symmetric and anti-symmetric conditions. The displacements of the flexible beam left end were set to zero, as is the case for a cantilever beam, while, at the other end, a vertical load F is applied. The optimization procedure is introduced in a dimensionless form similar to the parameterization proposed by De Bona and Munteanu, (2005). The dimensionless design parameters of the corner-filleted hinge take the form:

$$\beta = \frac{r}{l}, \quad \lambda = \frac{t}{l}, \quad \text{and } \omega = \frac{w}{l} \text{ : geometric parameters}$$

$$\mu = \frac{Fl}{\sigma_{adm} t^2 w}\text{: load parameter}$$

$$\nu = \frac{u_{max} E w t^2}{l^2 F}\text{: flexibility parameter}$$

where r, l, t, and w are the geometric parameters of the corner-filleted hinge with circular fillets and where σ_{adm}, and u_{max} are, respectively, the maximum yield strength of the selected material, and the maximum deflection of the hinge. In this case study, the geometric parameters are set to $\beta = 0.02$, $\lambda = 0.02$, and $\omega = 0.02$, and the load parameter is set to $\mu = 0.0134$. Figures 4.8a and b show, respectively, the mesh of the flexural beam and the refined meshing of one of the fillets where stress concentration occurs. The meshing was built with eight-node brick elements, which allow to capture the whole regime of stresses. Finally, the deformed position of the hinge, u_{max}, resulting from the application of the load F, is depicted in Fig. 4.7a

4.3.2 Objective Function and Constraints. The objective of the optimization procedure is to minimize the stress concentration at the transition between the fillet and the straight beam. A reference nominal stress is computed for a straight beam in pure bending. Since the beam has a constant rectangular cross-section of $w \times t$, the reference stress is not influenced by any change of curvature. When considering the case of pure bending as defined by Juvinall and Marshek (2000), the resulting stress is given by the equation:

$$\bar{\sigma} = \frac{Mc}{I} \tag{4.11}$$

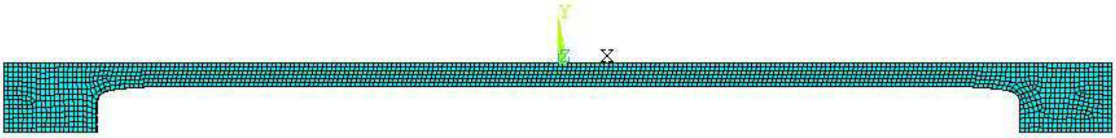

(A)

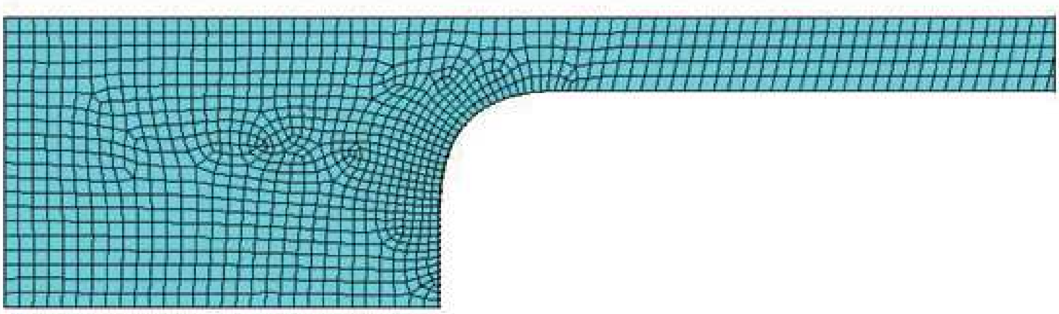

(B)

FIGURE 4.8. Meshing of the flexible beam: (a) front view; and (b) zoom-in on the fillet

where I is the moment of inertia of the cross section with respect to the neutral axis, and c is the distance from the neutral axis. For consistency with the location of the stress concentration, the nominal stress, represented by $\bar{\sigma}$, is computed with $c = t/2$ and $M = Fl$, which yields:

$$\bar{\sigma} = \frac{6Fl}{wt^2} \tag{4.12}$$

Thus, at the lower surface we have the reference stress state

$$\bar{\sigma}_1 = \bar{\sigma}, \qquad \bar{\sigma}_{vM} = \bar{\sigma} \tag{4.13}$$

where $\bar{\sigma}_1$ is the reference principal stress and $\bar{\sigma}_{vM}$ is the reference von Mises stress. The stress factors c_1 and c_{vM} are determined as relative to the nominal values, i.e.,

$$c_1 = \frac{\sigma_1}{\bar{\sigma}_1}, \qquad c_{vM} = \frac{\sigma_{vM}}{\bar{\sigma}_{vM}} \tag{4.14}$$

TABLE 4.1. Initial corner-filleted hinge

Profile	β	τ	ω	η	ν	c_{vM}	c_1
1	0.02	0.02	0.02	2.00	1743	4.42	4.61

where σ_1 and σ_{vM} are, respectively, the first principal and von Mises stress of the FE analysis of the flexible beam.

As the goal of a compliant hinge is to allow flexibility in the sensitive axis, the optimization of the stress concentration is obviously constrained by the stiffness of the flexible beam. If the flexible parameter ν classifies the characteristics of each hinge, the compliance constraint is defined by the expression

$$g(\mathbf{x}) = \nu - \nu_{adm} \geqslant 0 \tag{4.15}$$

where ν_{adm} is the deflection of the reference corner-filleted hinge. The flexibility constraint enables the optimization algorithm to discard solutions that are too stiff. Table 4.1 includes the properties of the initial corner-filleted hinge made of circular fillets.

4.4 Optimum Supercircular Fillet

The simplest shaped design that fulfils the G^2-continuity is a quarter of a super circular curve. Figure 4.6a shows the parameterization of the supercircular filleted hinge, where the five parameters, l, t, w, b, η are, respectively, the length, the thickness and the depth of the hinge, the height and power of the Lamé curve defined in eq. (4.5). It is noteworthy that the circular fillet is a specific case of the super circular fillet and, therefore, it has the same parameterization, with $r = b$ and $\eta = 2$.

The optimization problem consists in finding the power η that minimizes the stress concentration without decreasing the hinge compliance. Thus, the supercircular fillet problem is a single-variable optimization, where η is the design variable. The optimization problem is solved by minimizing the equation:

$$f(\eta) = (c_{vM})_{max} = \frac{(\sigma_{vM})_{max}}{\bar{\sigma}_{vM}} \to \min_{\eta} \tag{4.16}$$

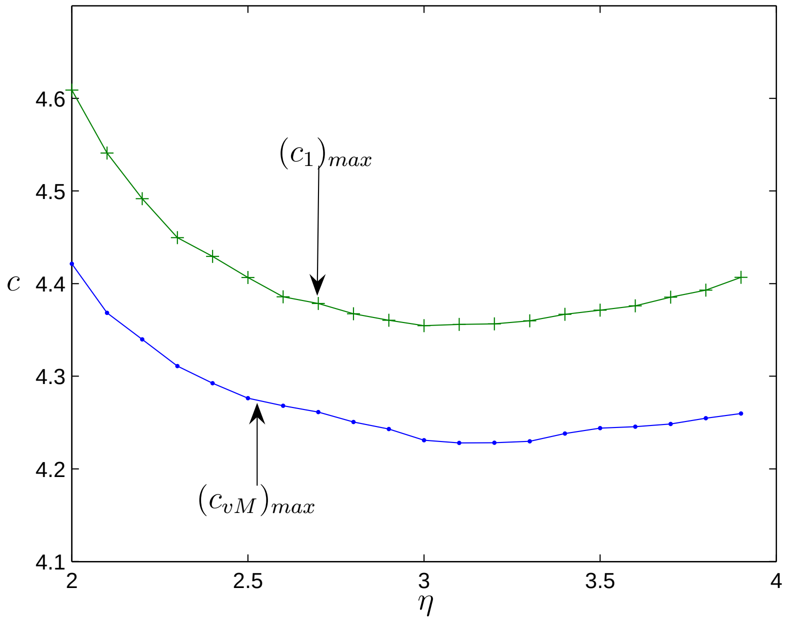

FIGURE 4.9. Stress concentration factor as a function of power η of a Lamé curve for supercircular fillet

subject the design constraint:

$$g(\eta) = \nu - \nu_{adm} \geqslant 0 \tag{4.17}$$

and to the boundary constraint:

$$2 < \eta \tag{4.18}$$

The FE analysis of the hinge with a supercircular fillet was conducted for different values of η. The resulting parametric study reveals the convex shape of the function describing the maximum stress concentration factor c as a function ofη. Thus, the minimum stress concentration is located at $\eta = 3.2$, as depicted in Fig. 4.9. The optimum design, for a minimax von Mises stress, is obtained for $\eta = 3.2$, which corresponds to a value of $\nu = 1797$, $(c_{vm})_{max} = 4.227$, and $(c_1)_{max} = 4.357$. To evaluate the influence of η on the stress concentration, we complete the parametric study with one digit of resolution. The resolution of the design variable η is limited by

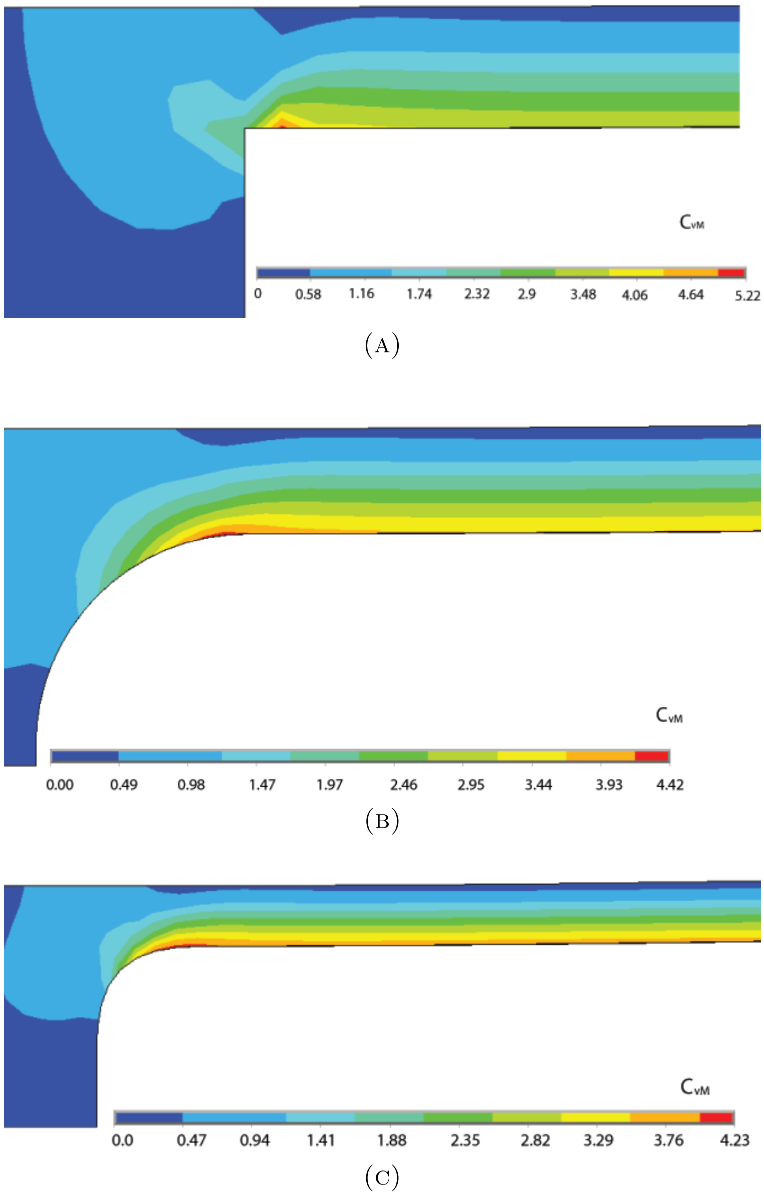

FIGURE 4.10. Von Mises stress distribution with (a) no fillet; (b) circular fillet; and (b) optimum supercircular fillet with $\eta = 3.2$

the accuracy of the FEA which depends on the mesh resolution. Therefore, to obtain a representative function $f(\eta)$, the size of the elements needs to be small enough to capture the small local change in geometry. Here, the element size has been refined to obtain the convex curves shown in Fig. 4.9.

Figures 4.10a, b, and c illustrate the stress fields of the rectangular, the circular, and the optimum supercircular hinge. Note that a square corner can be represented by a Lamé curve of infinite exponent ($\eta \to \infty$). Obviously, square corners are not good designs; traditionally, compliant hinges have been improved by mean of circular fillets. By removing material from the circular fillet, the maximum stress condition located around the fillets decreases with a stress concentration factor of $(c_{vM})_{max} = 4.421$ to $(c_{vM})_{max} = 4.227$, allowing an improvement of 4.4%. In addition, the flexibility parameter increases from $\nu_{adm} = 1743$ to $\nu = 1797$. This optimization demonstrates the improvement in the original shape of the corner-filleted hinge. Nevertheless, the supercircular fillet still has a limited shape domain for maximum stresses. This can be resolved by extending this domain further.

4.5 Optimum Superelliptical Fillet

A superelliptical fillet shape as an alternative to the supercircular fillet may be worthwhile because the new design improves even more the stress flow around the fillet of the compliant joint. However, an extra parameter is necessary to describe the elliptical shape of the new fillets. Figure 4.6b shows the parameterization of the superelliptic filleted hinge, b_x and b_y being the two scaling factors of eq. (4.5). The new optimization problem consists in minimizing the stress concentration of the superelliptical fillet, where the vector of design variables is expressed:

$$\mathbf{x} = [b_x \quad b_y \quad \eta]^T \tag{4.19}$$

The optimum superelliptical fillet is found as a solution of the problem:

$$f(\mathbf{x}) = (c_{vM})_{max} = \frac{(\sigma_{vM})_{max}}{\bar{\sigma}_{vM}} \to \min_{\mathbf{x}} \tag{4.20}$$

subject to the compliance constraint:

$$g(\mathbf{x}) = \nu - \nu_{adm} \geqslant 0 \tag{4.21}$$

and to the boundary constraints:

$$0 \leqslant x_1 \leqslant l/2, \qquad 0 \leqslant x_2, \qquad 2 < x_3, \tag{4.22}$$

which are set to respect the limitations of the geometry.

4.5.1 Optimization Algorithm. Problem (4.20) is of the constrained non linear type. Additionally, the objective function at hand is the maximum von Mises stress throughout the whole structural element, which is a non-analytic function of the design variables. This feature prevents the use of any gradient algorithm. To handle the non-analyticity of the objective function, we selected the Nelder-Mead simplex algorithm (Nelder and Mead, 1965). However, the original simplex algorithm does not handle constraints; therefore we use the simplex algorithm with a penalty function to handle the constraint. The modified simplex algorithm, outlined in Rahman (2006), is implemented in Matlab's Optimization toolbox. This implementation is used here.

To generate the FE model at each optimization step according to inputs of the simplex algorithm, a Matlab procedure was implemented, using Ansys as the simulation toolbox. This is feasible, since Matlab can execute any program without interrupting its processing. The procedure linking both softwares is depicted in Fig 4.11. First, Matlab most prepare the input file written in ANSYS parametric design language. Once the input file is created, ANSYS can be launched from Matlab using the *"dos"* command. Finally, by loading the FE analysis results to Matlab, Ansys is completely implemented in the optimization loop. Furthermore, Ansys automatically generates the mesh of the hinge at each optimization step.

4.5.2 Results. The results are recorded in dimensionless form, according to the notation:

$$\beta_x = \frac{b_x}{l},\ \beta_y = \frac{b_y}{l},\ \eta\text{: design parameters}$$

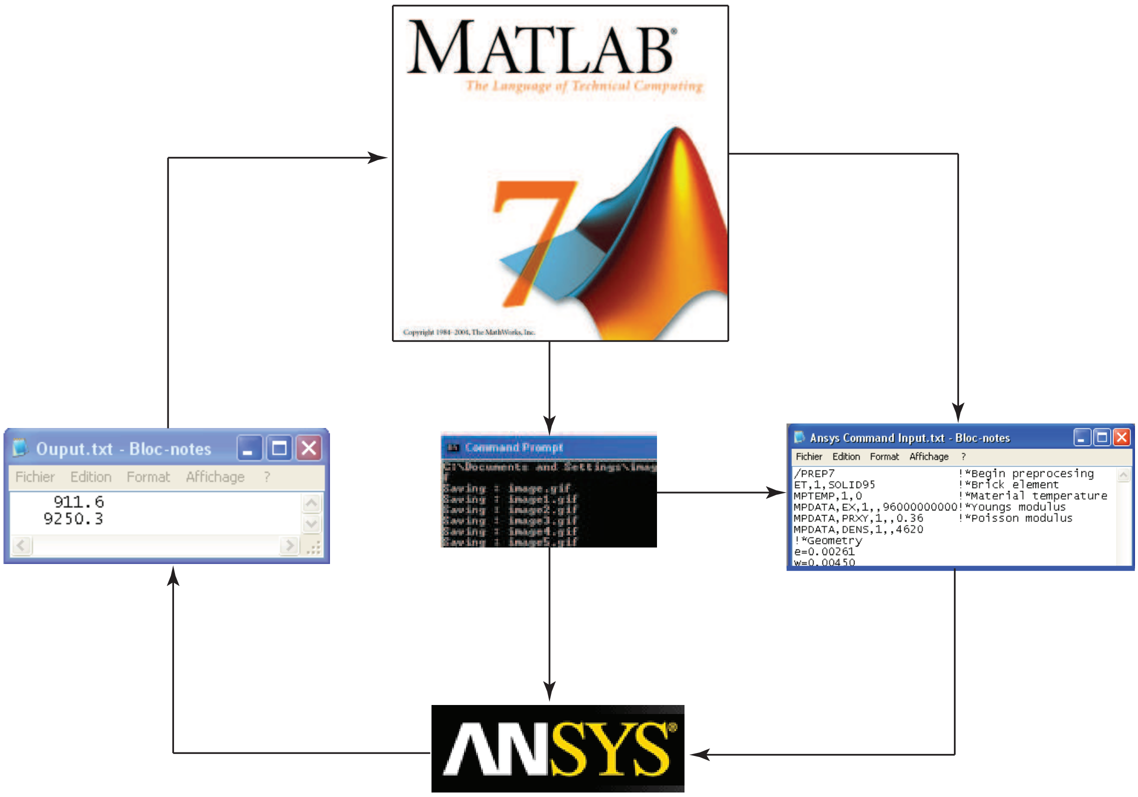

FIGURE 4.11. Link between Matlab and Ansys

The optimum superelliptical fillet for a flexible beam was found at a maximum stress concentration of $(c_{vM})_{max} = 3.656$, which is a substantive reduction, as opposed to the one provided by circular fillets. The correlating design parameters of the optimum superelliptical fillet correspond to $\beta_x = 0.5$, $\beta_y = 0.01$, and $\eta = 12.33$. The significant reduction in the stress concentration results from the improvement of the stress flow inside the flexible beam depicted in Fig. 4.12. In contrast to the circular fillets, where the stress is concentrated in a small area at the transition between the fillet and the straight line, the maximum von Mises stress of the superelliptical fillet is distributed along the flexible beam. The corresponding stress concentration distribution,c_{vM}, around the optimum fillet of the elliptical profile is shown in Fig. 4.12.

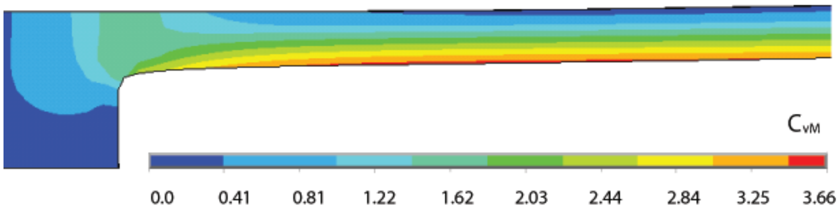

FIGURE 4.12. Von Mises stress concentration distribution of the optimum super elliptical fillet

TABLE 4.2. Summary of results

Profile	β_x	β_y	η	c_{vM}	ν	Improvement
0. No fillet	n.a.	n.a.	∞	5.217	1806	n.a.
1. Circular fillet	0.020	0.020	2.00	4.421	1688	n.a.
2. Optimum supercircular fillet	0.020	0.020	3.20	4.227	1762	4.4%
3. Optimum superelliptical fillet	0.500	0.010	12.33	3.656	1688	20.9%

4.6 Summary and Discussion

The suggested beam profiles are summarized in Table 4.2. The improvements in stress concentration of the two new profiles were computed in relation to the stress concentration of the original corner-filleted hinge profile. It is not surprising that profile 3 shows the greatest improvement. What is surprising is that profile 3 has an improvement of 20.9%, which is substantial in comparison with profile 2 improvement of 4.4%. Throughout the optimization, the design variable b_x converges to its upper boundary condition, causing the fillets of the hinge to merge, the straight portion of the beam thus vanishing. Therefore, the profile of the hinge is defined with a single formula. The optimum profile is also analytic everywhere.

The low stress concentration of profile 3 is obtained at the expense of a large power η that results in high curvature changes and, therefore, higher complexity (Khan, 2007). On the other hand, profile 2 has a higher stress concentration but much lower power η. Thus, the designer can make a compromise between stress concentration and complexity by selecting profile 2.

CHAPTER 5

Optimum Design of a Compliant Uniaxial Accelerometer

Optimization techniques are used in the design of compliant mechanisms. A popular technique is topology optimization, which can find the distribution of a given amount of material that maximizes the stiffness of the structure (Frecker et al., 1997; Bernardoni et al., 2004; Mankame and Ananthasuresh, 2004; Werme, 2007 ; Mechkour1 et al., 2007). The technique was originally developed to generate the architecture of optimum planar mechanisms. The problem with the resulting mechanism is that it does not consider the sensitivity to out-of-plane forces. Furthermore, this optimization technique cannot be used to find the optimum shape of a desired layout, since it generates its own layout.

The design technique introduced in this thesis does not generate optimum layouts, but optimizes the dimensions of a given layout. Thus, the designer is free to optimize any preselected three-dimensional compliant mechanism layout. Moreover, the technique minimizes the parasitic compliance in all off-axis directions. To do so, the a posteriori multi-objective algorithm is used to find the best trade-off between conflicting objective criteria of compliant mechanisms. Among the multi-objective optimization techniques, we have chosen the Normalized Normal Constraint algorithm to obtain an evenly distributed Pareto frontier (Messac et al., 2003).

The method is applied to the cross-configuration of the uniaxial simplicial architecture proposed by Cardou and Angeles (2007). We start with a general formulation of the optimization methodology; then, the method is applied to the uniaxial accelerometer of the foregoing reference.

5.1 The Optimization Methodology

This section describes the method used to find an optimum accelerometer architecture that minimizes the error of the measured acceleration. This error can be minimized by optimizing the sensitivity and natural frequencies of the compliant mechanism. The mechanical sensitivity evaluates the input-to-output amplification. In the field of compliant mechanisms, the input-to-output amplification ratio is called the *"mechanical advantage"* and it is defined by Lobontiu (2003) as:

$$m.a. = \frac{|u_{out}|}{|u_{in}|} \tag{5.1}$$

where u_{in} and u_{out} are the input and output linear or angular displacement. Regarding accelerometers, the output displacement is not generated by an input displacement but with an input acceleration (a_{in}). Hence, we define here the mechanical sensitivity of an accelerometer as

$$\Upsilon(\mathbf{x}) = \frac{|u_{out}(\mathbf{x})|}{|a_{in}|}, \tag{5.2}$$

where $|a_{in}|$ is the amplitude of a step input and $|u_{out}(\mathbf{x})|$ is the steady-state value of the displacement response. On the other hand, a minimum parasitic compliance in the plane normal to the sensitive axis, which is inversely proportional to the second natural frequency λ_s, can be obtained by minimizing the ratio between the first and the second natural frequencies. Finally, the axis drift needs to be taken into account only when the stiffness of the plane orthogonal to the sensitive axis is not isotropic. In the case of anisotropic stiffness, the resulting inertia forces acting on the system will not be balanced and will make the proof-mass deflect outside its translation trajectory. Designers need to ensure elastic isotropy in the normal plane by suitably specifying the layout of the accelerometer. Thus, the optimization problem can be described as:

$$\mathbf{f}(\mathbf{x}) \equiv \begin{bmatrix} 1/|\Upsilon(\mathbf{x})| \\ \lambda_l(\mathbf{x})/\lambda_s(\mathbf{x}) \end{bmatrix} \rightarrow \min_{\mathbf{x}} \tag{5.3}$$

subject to boundary constraints

$$x_j^l \leqslant x_j \leqslant x_j^h \tag{5.4}$$

and the design constraints

$$g_1(\mathbf{x}) \leqslant 0, \qquad g_2(\mathbf{x}) \leqslant 0 \tag{5.5}$$

where

$$\mathbf{x} = [x_1, x_2, \ldots, x_j, \ldots, x_N] \tag{5.6}$$

The boundary constraints limit the geometric variables to acceptable values defined by the manufacturing process. On the other hand, the design constraints deal with the maximum design space and the strength requirement of the mechanism. The first constraint is a limit to the volume L^2H defined by the length and width of the mechanism. The second constraint restricts the stress in the flexible element of the accelerometer to fall in a range of $\pm 1000\ g$ of measurable acceleration. Within this range, the mechanism strain is prevented from plastic deformation. To compute the natural frequencies at every optimization step, a finite element solver was coupled with the optimization algorithm. Thus, before conducting the multi-objective optimization, the model analysis must first be performed as shown in Fig. 5.1, where the steps of the optimization procedure are embedded within the design process.

5.2 Problem Formulation

The parameters depicted in Fig. 5.2 describe the structure of the accelerometer. To optimize the layout of the accelerometer, seven parameters of the layout adopted

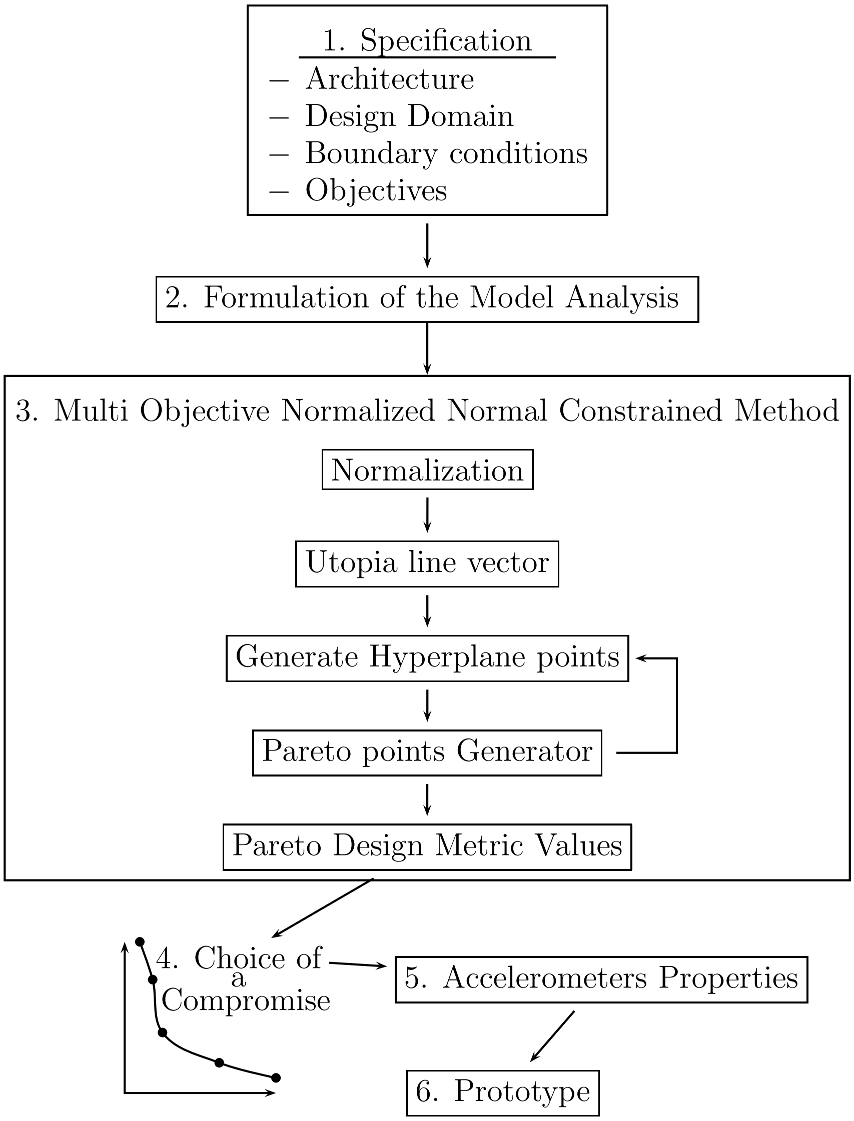

FIGURE 5.1. Methodology flow chart

are considered as design variables and arrayed in the design vector $\mathbf{x}$:

$$\mathbf{x} = [w \quad e \quad t \quad l \quad b_x \quad b_y \quad \eta]^T \tag{5.7}$$

where w, e, t, l, b_x, b_y, and η represent, respectively, the width and length of the proof-mass, the thickness and length of the compliant joint, and the height, length, and degree of the Lamé curves describing the fillets of the compliant hinges.

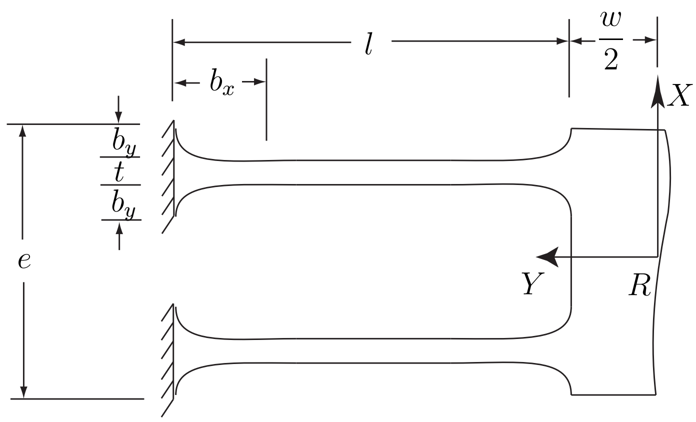

FIGURE 5.2. Parameterization of the cross-configuration mechanism

The symmetric configuration of the accelerometer rules out the axis-drift of the compliant mechanism. Therefore, we have a bi-objective optimization, the objectives being the sensitive-axis and the off-axis stiffness. The optimization problem is defined as:

$$\mathbf{f}(\mathbf{x}) = \begin{bmatrix} f_1(\mathbf{x}) \\ f_2(\mathbf{x}) \end{bmatrix} \equiv \begin{bmatrix} 1/\Upsilon(\mathbf{x}) \\ \lambda_l(\mathbf{x})/\lambda_s(\mathbf{x}) \end{bmatrix} \to \min_{\boldsymbol{x}} \tag{5.8}$$

subject to the boundary constraints:

$$0 \leqslant x_1, \qquad (4b + 2t) \leqslant x_2 \tag{5.9a}$$

$$\epsilon \leqslant x_3, \qquad 0 \leqslant x_4 \tag{5.9b}$$

$$0 \leqslant x_5 \leqslant l/2 \tag{5.9c}$$

$$2\epsilon \leqslant x_6, \qquad 2 < x_7 \tag{5.9d}$$

and the design constraints:

$$g_1(\mathbf{x}) = \frac{(2l + w)^2 e}{L^2 H} - 1 \leqslant 0, \qquad g_2(\mathbf{x}) = \max(\sigma_{vM} - \sigma_{adm}) \leqslant 0 \tag{5.10}$$

where $\lambda_l(\mathbf{x})$, $\lambda_s(\mathbf{x})$, σ_{vM}, and σ_{adm} are, respectively, the first and second natural frequency, the von Mises stress and the admissible stress for the maximum acceleration of 1000 g.

The optimization problem is subjected to the boundary constraints imposed by the physical dimensioning of the compliance mechanism, except for x_3 and x_6, which are limited by the Direct Metals Laser-Sintering (DMLS) machine tool resolution (Chapter 2). Indeed, the joint thickness t cannot be smaller than the smallest focus diameter, $\epsilon = 100\ \mu$m. On the other hand, $g_1(\mathbf{x})$ describes the compactness, which is subject to an inequality constraint to limit the design space. This limit is identified by a box with volume $L^2H = 10^3\text{mm}^3$. Finally, to compute the stress constraint $g_2(\mathbf{x})$ and the natural frequencies of the device, a Matlab routine was implemented to call the FEA solver at each optimization step. Figure 5.3 shows the mesh of the accelerometer for the modal analysis. In the case of the stress constraint $g_2(\mathbf{x})$, we use a different mesh which considers the symmetries of the accelerometer. Since the compliant joints are all equally loaded, we computed the stress in only one hinge. The structural model can be simplified even more with an symmetric analysis of the compliant joint. Figure 5.4 shows the model used for the structural analysis and the plane subjected to the anti-symmetric condition. Recall that an anti-symmetry condition applies when only the geometry is symmetric with respect to an axis. The displacements of the flexible beam left end were set to zero, while, at the other end, the rotations and displacement in the neutral axis direction where set to zero in order to respect the layout of the accelerometer. The load case is also depicted in Fig. 5.4 where the bending load is set to

$$F = a_{in}\frac{m_p}{n} = \frac{1000gw^2e\rho}{8} \tag{5.11}$$

where a_{in}, m_p, n, g, and ρ are, respectively, the maximum acceleration input, the mass of the proof-mass, the number of compliant links, the gravity constant, and the density of the titanium alloy.

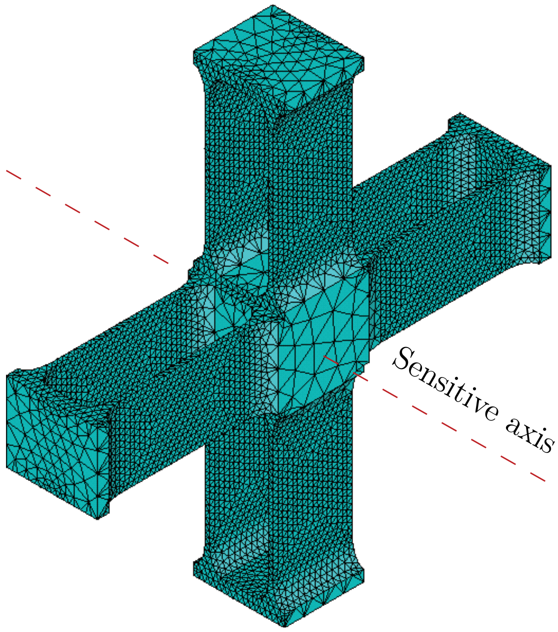

FIGURE 5.3. FE model of the accelerometer

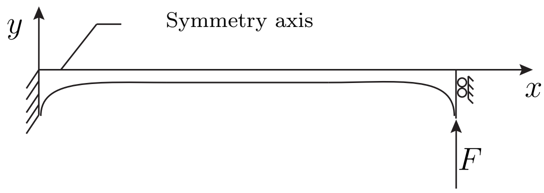

(A)

FIGURE 5.4. Structural model

5.3 Multi-objective Formulation

The non-analytical nature of the modal analysis prevents us from using gradient-based methods. To overcome this issue, we use a direct method. In the field of optimization, the Nelder-Mead simplex algorithm (Nelder and Mead, 1965) is a well-known effective method for direct-search optimization. Recall that a simplex is a set of $(n+1)$ affinely independent points in $\mathbb{R}^n$ (Kreyszig, 1997). The Nelder-Mead simplex algorithm is also the basis of the intelligent moving object optimization algorithm (INTEMOB), proposed by Rahman (2006), due to its capability to handle non-differentiable, discontinuous, and non-analytical functions. The original simplex

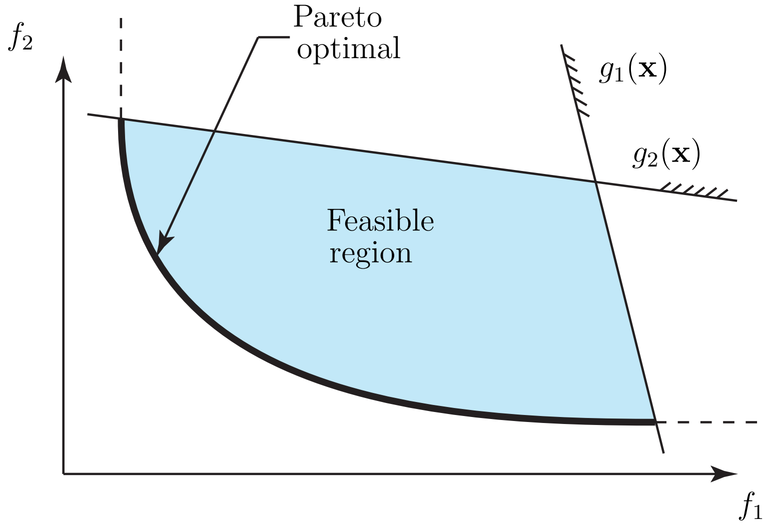

FIGURE 5.5. Bi-objective design space

algorithm, however, does not handle constraints. On the other hand, the Rahman's algorithm handles constraints.

Bearing in mind that INTEMOB is able to operate only on a single objective function for minimization, we resort to multi-objective optimization, which is the process of simultaneously optimizing two or more conflicting objectives subject to certain constraints. As we have a bi-objective case, the feasible region of the design space is represented in a plot where the coordinate axes are the two objective functions, as depicted in the Fig 5.5. Multi-objective problems are known to have not one but many solutions, which form the Pareto optimal set or Pareto frontier. A Pareto solution is one where any improvement in one objective can only occur by worsening one or many other objectives. For the bi-objective optimization, the Pareto optimal set forms a curve of optimum compromise, as show in Fig 5.5.

We selected the Normalized Normal constraint method, proposed by Messac et al. (2003), to generate the Pareto frontier over the high number of multi-objective algorithm (Marler and Arora, 2004). The Normalized Normal Constraint Method (NNCM) is a significant advancement in the field of multi-objective optimization because it generates a set of evenly spaced solutions on a normalized Pareto frontier. The method for the bi-objective case comprises seven steps.

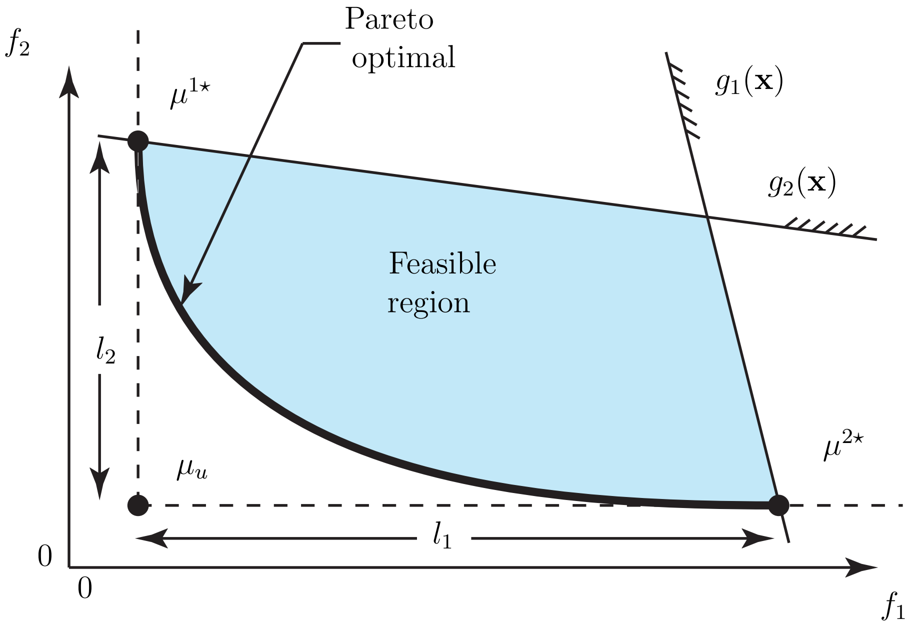

FIGURE 5.6. Pareto frontier

Step 1: ANCHOR POINTS. To normalize the two-dimensional Pareto frontier, we first need to find the two anchor points, $\mu^{1\star}$ and $\mu^{2\star}$, which are the solutions minimizing both objectives independently. The line joining the two anchor points is called the Utopia line. The anchor points are obtained by solving problem PU1 and PU2, defined below, with the INTEMOB algorithm:

Problem PUi $\qquad$ $(i = 1, 2)$

$$f_i(\mathbf{x}) \to \min_{\boldsymbol{x}} \tag{5.12}$$

subject to the boundary constraints

$$x_{lj} \leqslant x_j \leqslant x_{uj} \qquad (j = 1, 2, \ldots, N) \tag{5.13a}$$

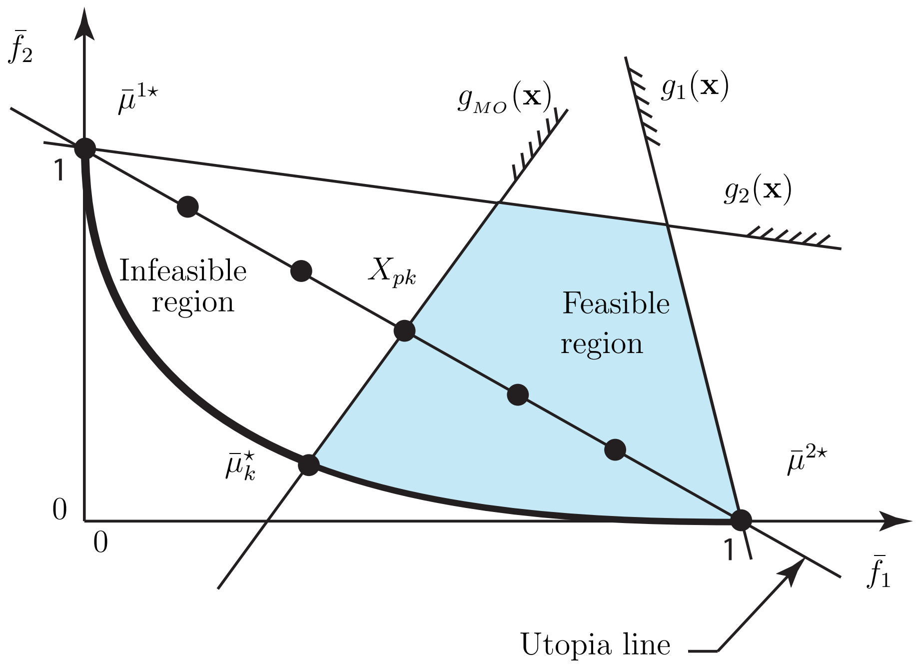

FIGURE 5.7. Normalized pareto frontier

and the design constraints

$$g_1(\mathbf{x}) \leqslant 0, \qquad g_2(\mathbf{x}) \leqslant 0 \tag{5.14}$$

with $f_1(\mathbf{x})$ and $f_2(\mathbf{x})$ defined, respectively, as the first and the second objective functions of eq. (5.3).

Step 2: OBJECTIVE MAPPING. To avoid scaling deficiencies, the optimization takes place in the normalized design objective space. Utopia point μ_u of Fig. 5.6 is defined as

$$\mu_u = \{f_1(\mathbf{x}^{1\star}) \quad f_2(\mathbf{x}^{2\star})\} \tag{5.15}$$

and the distances l_1 and l_2 of Fig. 5.6 as

$$l_1 = f_1(\mathbf{x}^{2\star}) - f_1(\mathbf{x}^{1\star}) \tag{5.16}$$

$$l_2 = f_2(\mathbf{x}^{1\star}) - f_2(\mathbf{x}^{2\star}) \tag{5.17}$$

If $\bar{f}$ is the normalized form of f, the normalized design space displayed in Fig. 5.7 can be evaluated as

$$\bar{\mathbf{f}}(\mathbf{x}) = \left[\frac{f_1(\mathbf{x}) - f_1(\mathbf{x}^{1\star})}{l_1} \quad \frac{f_2(\mathbf{x}) - f_2(\mathbf{x}^{2\star})}{l_2}\right]^T \tag{5.18}$$

Step 3: UTOPIA LINE VECTOR. Define $\bar{\mathbf{n}}_u$ as the vector directed from $\bar{\mathbf{f}}(\mathbf{x}^{1\star})$ to $\bar{\mathbf{f}}(\mathbf{x}^{2\star})$, yielding

$$\bar{\mathbf{n}}_u = \bar{\mathbf{f}}(\mathbf{x}^{2\star}) - \bar{\mathbf{f}}(\mathbf{x}^{1\star}) \tag{5.19}$$

Step 4: NORMALIZED INCREMENTS. Compute a normalized increment δ along the direction $\bar{\mathbf{n}}_u$ for a prescribed number of solutions, m_1, as

$$\delta = \frac{1}{m_1 - 1} \tag{5.20}$$

Step 5: GENERATE UTOPIA LINE POINTS. Evaluate a set of vectors $\bar{\mathbf{x}}_{pk}$ which define $\bar{\mathcal{X}}_{pk}$, the set of evenly distributed points on the Utopia line (Fig. 5.7).

$$\bar{\mathbf{x}}_{pk} = \iota_{1k}\bar{\mathbf{f}}(\mathbf{x}^{1\star}) + \iota_{2k}\bar{\mathbf{f}}(\mathbf{x}^{2\star}) \tag{5.21}$$

where

$$\iota_{1k} + \iota_{2k} = 1 \qquad 0 \leq \iota_{1k} \leq 1 \tag{5.22}$$

Note that ι_{ik} is incremented by δ between 0 and 1 for $k \in \{1, 2, ..., m_1\}$.

Step 6: PARETO POINT GENERATION. Based on the new normalization we find the other $m_1 - 2$ Pareto solutions using the set of evenly distributed points on the Utopia line. For each point generated on the Utopia line, we solve

Problem Pk (for $k = 2, 3, 4, ..., m_1 - 1$)

$$f_2(\mathbf{x}) \rightarrow \min_{x} \tag{5.23}$$

subject to the boundary constraints

$$x_{lj} \leqslant x_j \leqslant x_{uj}, \qquad j = 1, 2, \ldots, N \tag{5.24a}$$

the design constraints

$$g_1(\mathbf{x}) \leqslant 0, \qquad g_2(\mathbf{x}) \leqslant 0, \tag{5.25}$$

and the new multi-objective constraint

$$\bar{\mathbf{n}}_u^T(\bar{\mathbf{f}}(\mathbf{x}) - \bar{\mathbf{x}}_{pk}) \leq 0. \tag{5.26}$$

Step 7: PARETO DESIGN. Finally, the design solution that corresponds to each Pareto point can be evaluated in the design space by the relation

$$\mathbf{f}(\mathbf{x}_k) = [l_1\bar{f}_1(\mathbf{x}_k) + f_1(\mathbf{x}^{1\star}) \qquad l_2\bar{f}_2(\mathbf{x}_k) + f_2(\mathbf{x}^{2\star})]^T \tag{5.27}$$

5.4 RESULTS

To define the normalized Pareto optimal set, the two anchor points, $\mu^{1\star}$ and $\mu^{2\star}$, were obtained by solving problems PU1 and PU2 with the INTEMOB algorithm. At the optimum points, $\mathbf{x}^{1\star} = [2.7 \quad 2.3 \quad 0.1 \quad 9.2 \quad 0.2 \quad 80/9]^T$ and $\mathbf{x}^{2\star} = [4.5 \quad 5.9 \quad 0.1 \quad 4.5 \quad 0.2 \quad 43/9]^T$, we found the two anchor points $\mu^{1\star} = \{2.50 \times 10^7 \quad 0.1378\}$ and $\mu^{2\star} = \{9.17 \times 10^7 \quad 0.0452\}$. Thus, the Utopia point results to be $\mu_u = \{2.50 \times 10^7 \quad 0.0452\}$.

TABLE 5.1. Pareto solutions

k	ι_{1k}	ι_{2k}	Υ (nm/g)	$\lambda_l(\mathbf{x})$ (Hz)	$\dfrac{\lambda_l(\mathbf{x})}{\lambda_s(\mathbf{x})}$	w (mm)	e (mm)	t (mm)	l (mm)	b_x (mm)	b_y (mm)	η
1	1.00	0.00	40.12	834.7	0.1378	2.71	2.31	0.10	9.12	4.12	0.20	80/9
2	0.83	0.17	35.61	914.3	0.1056	4.57	2.62	0.10	7.45	3.37	0.20	7
3	0.67	0.33	27.92	1029	0.0840	5.62	2.75	0.10	6.70	3.01	0.20	67/11
4	0.50	0.50	21.94	1145	0.0713	5.51	3.21	0.10	6.01	2.71	0.20	23/4
5	0.33	0.67	16.72	1301	0.0623	5.23	4.11	0.10	5.18	2.32	0.20	16/3
6	0.17	0.83	13.25	1526	0.0540	4.91	4.92	0.10	4.82	2.19	0.20	5
7	0.00	1.00	10.97	1855	0.0424	4.49	5.87	0.10	4.51	2.02	0.20	43/9

$$\text{ProblemPU1}: \qquad f_1(\mathbf{x}) = 1/|\Upsilon| \to \min_{\mathbf{x}} \tag{5.28}$$

subject to eqs. (5.9) and (5.10)

$$\text{ProblemPU2}: \qquad f_2(\mathbf{x}) = \frac{\lambda_l}{\lambda_s} \to \min_{\mathbf{x}} \tag{5.29}$$

subject to eqs. (5.9) and (5.10)

In addition to the anchor points, we need to find five additional solutions of the Pareto frontier to determine a total of seven points. Consequently, the interval distance on the Utopia line is equal to $\delta = 0.1666$. The Pareto optimum solutions are listed in Table 5.1; Fig. 5.8 depicts the corresponding Pareto frontier. Note that each solution satisfies all the optimization constraints.

The Pareto frontier gives freedom to select a design layout to meet specific conditions of the accelerometer. At one extreme, i.e. point 1, of the Pareto frontier, the

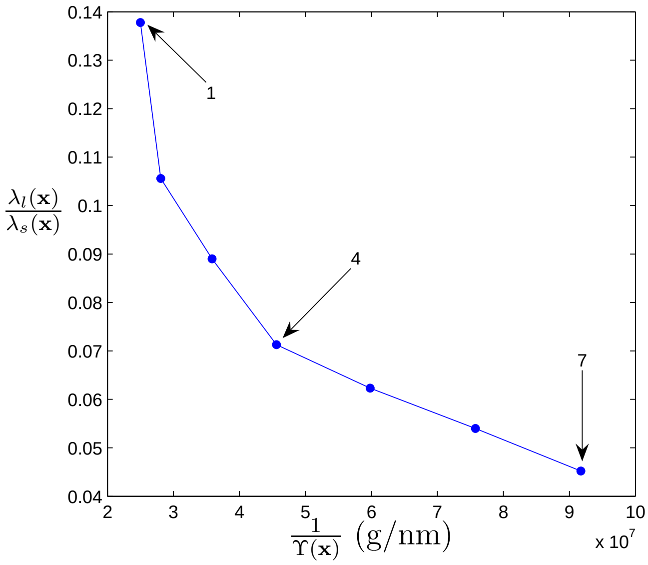

FIGURE 5.8. Pareto frontier

fundamental frequency is the lowest and corresponds to the most sensitive accelerometer. At the other extreme, point 7, the frequency ratio $\lambda_l(\mathbf{x})/\lambda_s(\mathbf{x})$ is a minimum. The structural parameters that correspond to this point are the most appropriate for low parasitic-sensitivity accelerometers.

All the other points are intermediate optimum solutions that also satisfied the the optimization constraints. The seven Pareto solutions correspond to optimum accelerometers with different specifications. They are selected with respect to the weight factor related to the application of the accelerometer. As stated in section 1.1, we aim at a general case where the accelerometer should have a natural frequency slightly higher than 1000 Hz and a ratio lower than 1/10. We pick solution 4 of Fig. 5.8 as it is the first point that meets the two conditions. The fundamental frequency and the frequency ratio correspond, respectively, to 1145 Hz and 0.0727. Figures 5.9 and 5.10 depict, respectively the accelerometer layout and stress flow of solution 4.

To verify the relative sensitivity of the accelerometer in the three orthogonal axes, we resort to FEA to calculate the deflection of the proof mass in the principal

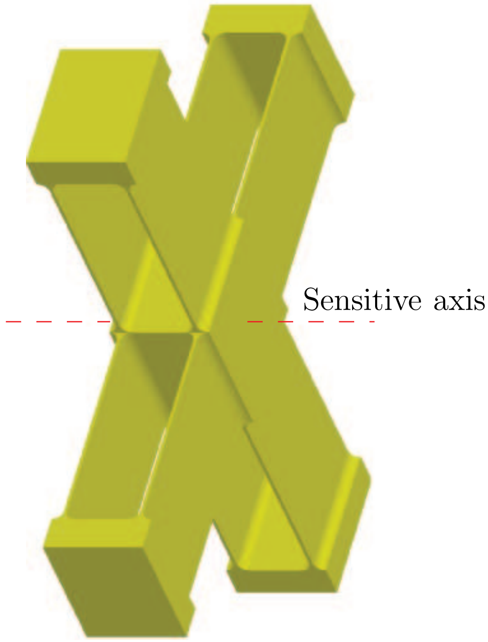

FIGURE 5.9. Optimum accelerometer

TABLE 5.2. Sensitivity of the accelerometer

acceleration	Proof mass deflection (nm)		
	X axis	Y axis	Z axis
$a_x = 1g$	22	7.4×10^{-4}	5.5×10^{-4}
$a_y = 1g$	4.8×10^{-4}	3.5×10^{-2}	3.0×10^{-4}
$a_z = 1g$	2.6×10^{-4}	2.7×10^{-4}	3.9×10^{-2}
$a_y = a_z = 0.707g$	5.1×10^{-3}	9.7×10^{-3}	9.7×10^{-3}

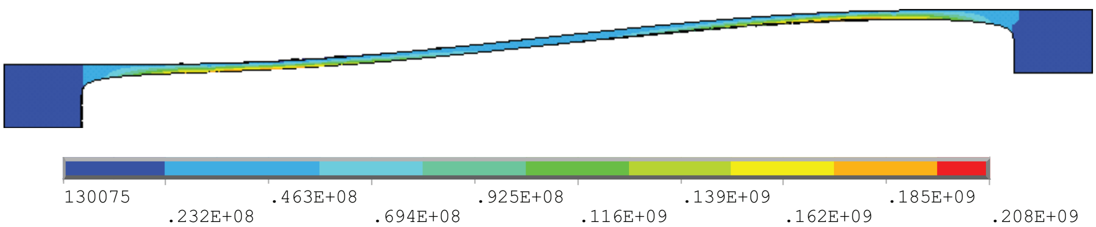

FIGURE 5.10. Von Mises stress distribution

direction. The results are listed in Table 5.2 and show that the accelerometer is 10^3 times more compliant in the sensitive axis than in the other directions.

5.5 DISCUSSION

The NNCM algorithm determines a good approximation of the Pareto frontier with a small number of optimum solutions; this is a considerable advantage for mechanical systems with high computational complexity. In the problem at hand, only seven solutions were obtained to approximate well the Pareto frontier. The solutions are equally distributed along the Utopia line, as opposed to a priori multi-objective optimization methods, which need a larger number of points to represent the Pareto frontier.

The Pareto frontier helps the designer select the best compromise among a set of optimum designs. In our case, we choose solution 4 as the resulting accelerometer met the general characteristics of a low-frequency accelerometer with a usable frequency range that goes from 0 to 600 Hz. Low-frequency accelerometers have the advantage of a high sensitivity and good compactness; however, they have the disadvantages of a very fragile mechanical structure and high off-axis sensitivity. Thus, commonly used low-frequency accelerometers have a limited range of acceleration between 1 g and 50 g and high off-axis sensitivity of around 5%. To overcome these problems, the accelerometer layout was optimized by considering these four characteristics. The first objective of the multi-objective optimization is to maximize the mechanical sensitivity (Υ) of the accelerometer. However, by minimizing $1/\Upsilon$ and the ratio of frequency λ_f/λ_s , the optimization also affects the accelerometer usable frequency range, which cannot exceed 1/3 of its natural frequency. Since the optimum accelerometer has a natural frequency of 1145 Hz, its usable frequency ranges from 0 to 381 Hz. Moreover, the proposed compliant mechanism exhibits a low mechanical off-axis sensitivity through the minimization of the second objective. The resulting compliant mechanism is at least 1000 times more sensitive in its sensitive axis than in the other directions, which is a significant improvement. Finally, the optimization constraints allow the mechanism to fit in a box of $17.5 \times 17.5 \times 3.2$ mm^3, and prevent failure of the compliant mechanism under ± 1000 g.

The optimization requires several runs before converging toward a global minimum. In order to converge, the algorithm requires a good compromise between the mesh resolution and the convergence criterion. A high mesh resolution needs larger computation time, while a coarse mesh will not represent the objective function correctly. The convergence criterion is to be set to the required degree of accuracy of the FEA. The overall CPU cost of the algorithm is very large because the objective functions are computed with a high resolution meshing. Several hours were necessary to compute only one Pareto solution.

CHAPTER 6

Closing Remarks

6.1 Conclusions

The optimum design of a compliant simplicial uniaxial accelerometer (SUA) was reported in this thesis.

First, in Chapter 2, we described in detail the characteristics of compliant mechanisms and the compliant realization of the original layout of the SUA. We selected the material with properties maximizing the inertial sensor performance.

The advantages and shortcomings of compliant mechanisms were highlighted in Chapter 3 by conducting the kinematic analysis of three different systems. A lumped-parameter model was first tested to solve a simple system made of one notched beam and one mass. Afterwards, the lumped-parameter model was used to highlight the deficiencies of the original layout of the SUA. To cope with the low off-axis stiffness and the axis-drift of the SUA, we came up with an new alternative layout.

One of the drawbacks affecting compliant mechanisms is the stress concentration which limits the range of motion and life cycle of the mechanism. In Chapter 4, we proposed a new compliant hinge design to decrease the stress concentration. We called this new hinge Lamé-shaped hinge as we used Lamé curves to produce the profile of the hinge. The advantages of Lamé curves were demonstrated by studying the curvature of the profile of compliant hinges and mostly by optimizing the profile of the Lamé-shaped hinge. In this particular optimization problem, the objective function was defined as the maximum stress concentration subject to a flexibility constraint. We found an improvement of up to 20% over the original corner-filleted hinge of equal compliance.

The Normalized Normal Constraint Method, which is a multi-objective algorithm, was applied in Chapter 5 to accelerometer design. Although only two objective functions were considered, the method can readily be extended to multiple objective functions. The method was applied to optimize the new layout of the simplicial uniaxial accelerometer. The solution found gives an accelerometer with excellent stiffness and strength properties compared to the initial mechanism (Chapter 2). The stress flow is improved by using a superelliptical fillet, and the overall volume of the device is now 1/3 of the initial layout. In addition, the first natural frequency went from 1679 Hz to 1145 Hz, improving the sensitivity of the accelerometer. Therefore, the usable frequency range of the final accelerometer goes from 0 Hz to 380 Hz. Finally, the ratio of frequency went from 0.125 to 0.0727; thus, there is now more than one order of magnitude between the two lowest frequencies. We have thus reached our design objectives.

6.2 Recommendations for Future Work

As an extension to the work reported here, several issues remain to be further explored:

(*i*) The Bode diagrams and the complex frequency responses in the three orthogonal axis of the proof mass need to be computed;

(*ii*) The fabrication process of the accelerometer is to be conducted;

(*iii*) Compute the mounted frequency of the accelerometer by including the rigidity of the accelerometer frame;

(*iv*) The compliant realization of the Simplicial Triaxial Accelerometer is to be designed by adding a notched beam at each end of the compliant ΠΠ-legs layout proposed in Chapter 2.

BIBLIOGRAPHY

Algrain, M. C. and Quinn, J. (1993), Accelerometer based line-of-sight stabilization approach for pointing and tracking systems, *in* 'In Proceedings of 2nd IEEE Conference on Control Applications', Vancouver, Canada, pp. 159–163.

Ananthasuresh, G. and Kota, S. (1995), 'Designing compliant mechanisms', *Mechanical Engineering* **68**(3), 93–96.

Angeles, J. (2004), 'The qualitative synthesis of parallele manipulators', *ASME Journal of Mechanical Design* **126**(4), 617–624.

Angeles, J. (2007), *Fundamentals of Robotic Mechanical Systems. Theory, Methods, and Algorithms*, 3rd edn, Springer, New York.

Arai, T., Hervé, J. M. and Tanikawa, T. (1996), Development of 3 dof micro finger, *in* 'Proceedings of IROS Conference', Vol. 96, Osaka, Japan, pp. 981–987.

Ashby, M. F. (2005), *Materials Selection in Mecanical Design*, 3nd edn, Elsevier Butterworth Heinemann: Amsterdam.

Bao, M. (2000), *Micro mechanical transducers : pressure sensors, accelerometers, and gyroscopes*, Elsevier Butterworth Heinemann: Amsterdam.

Bernardoni, P., Bibaud, P., Bidard, C. and Gosselin, F. (2004), 'A new compliant mechanism design methodology based on flexible building blocks', *Smart Structures and Materials 2004. Modeling, Signal Processing, and Control* **5383**(1), 244–254.

Cardou, P. (2007), Design of Multiaxial Accelerometers with Simplicial Architectures for Rigid-Body Pose and Twist Estimation, PhD thesis, McGill University, Montreal, Canada.

Cardou, P. and Angeles, J. (2007), Simplectic architectures for true multi-axial accelerometers: A novel application of parallel robots, *in* 'IEEE International Conference on Robotics and Automation', Roma, Italy, pp. 181–186.

Cardou, P., Pasini, D. and Jorge, A. (2008), 'Lumped elastodynamic model for mems: Formulation and validation', *IEEE Journal of Microelectromechanical Systems* .

De Bona, F. and Munteanu, M. G. (2005), 'Optimized flexural hinges for compliant micromechanisms', *Springer Science* **44**, 163–174.

Derderian, A. M., Howell, L., Murphy, M. D., Lyon, S. M. and Pack, S. D. (1996), Compliant parallel-guiding mechanisms, *in* 'Proceding of the 1996 ASME Design Engineering Technical Conference', Vol. 96, Irvine, CA, USA.

Dunn, M., Suwito, W. and Cunningham, S. (1997), 'Stress intensities at notch singularities', *Egineering Fracture Mechanics* **57**(4), 417–430.

Frecker, M., Ananthasuresh, G., Nishiwaki, S., Kikuchi, N. and Kota, S. (1997), 'Topological synthesis of compliant mechanisms using multi-criteria optimization.', *ASME Journal of Mechanical Design* **119**, 238–245.

Gray, A. (1993), *Modern Differential Geometry of Curves and Surfaces*, CRC Press: Boca Raton.

Howell, L. (2001), *Compliant Mechanisms*, J. Wiley & Sons: New York.

Juvinall, R. and Marshek (2000), *Fundamentals of Machine Component Design*, 3nd edn, John Wiley & Sons, Inc.

Khan, W. A. (2007), The Conceptual Design of Robotic Architectures Using Complexity Criteria, PhD thesis, McGill University, Montreal, Canada.

Kreyszig, E. (1997), *Advanced Engineering Mathematics*, 8nd edn, John Wiley & Sons: New York.

Kruglick, E., Warneke, B. and Pister, K. (1998), 'Cmos 3 -axis accelerometers with integrated amplifier', *IEEE* pp. 631–636.

Li, G., Li, Z., Wang, C., Hao, Y., Zhang, D. and Wu, G. (2007), 'Design and fabrication of a highly symmetrical capacitive triaxial accelerometer', *Journal of Micromechanics and Microengineering* **17**, 36–41.

Lobontiu, N. (2003), *Compliant Mechanisms: Design of Flexure Hinges*, CRC Press: Boca Raton, FL, USA.

Lobontiu, N. and Garcia, E. (2003), 'Analytical model of displacement amplification and stiffness optimization for a class of flexure-based compliant mechanisms', *Science Direct* **81**, 981–987.

Lobontiu, N. and Garcia, E. (2005), 'Circular-hinges line element for finite element analysis of compliant mechanisms', *Journal of Mechanical Design* **127**, 766–773.

Lobontiu, N., Garcia, E., Hardau, M. and Bal, N. (2004), 'Stiffness characterization of corner-filleted flexure hinges', *Review of scientific instruments* **75**(11), 4896–4904.

Loria, G. (1902), *Spezielle Algebraische und Transscendente Ebene Kurven: Theorie und Geschichte,*, BG Teubner: Leipzig.

Macdonald, G. (1990), 'Review of low cost accelerometers for vehicle dynamics.', *Sensors Actuators* **A**(21), 303307.

Mankame, N. and Ananthasuresh, G. (2004), 'Topology synthesis of electrothermal compliant mechanisms using line elements.', *Structural Multidisciplinairy Optimization* **26**, 209218.

Marler, R. and Arora, J. (2004), 'Survey of multi-objective optimizatoin methods for engineering', *Structural Multidisciplinary Optimization* **26**, 369–395.

Mechkour1, H., Jouve, F., Rotinat-Libersa, C., Bidard3, C. and Perrot, Y. (2007), Optimal design of compliant mechanisms by level set and flexible building blocks methods, *in* '7th World Congress on Structural and Multidisciplinary Optimization', Seaoul, Korea, pp. 1898–1907.

Messac, A., Ismail-Yahaya, A. and Mattson, C. (2003), 'The normalized normal constraint method for generationg the pareto frontier', *Structural Multidisciplinary Optimization* **25**(2), 86–98.

Mineta, T., Kobayashi, S., Watanabe, Y., Kanauchi, S., Nakagawa, I., Suganuma, E. and Esahi, M. (1996), 'Three-axis capacitive accelerometer with uniform axial sensitivities', *Journal of Micromechanics and Microengineering* **6**, 631–635.

Moaveni, S. (2003), *Finite Element Analysis: Theory and Application with Ansys*, 2nd edn, Pearson Education, Upper Saddle River, New Jersey, USA.

Moon, Y., Trease, P. and Kota, S. (2002), Design of large-displacement compliant joints, *in* 'MECH 27th Biennial Mechanisms and Robotics Conference', number 3, Montreal, Canada.

Navid, Y., Najafi, K. and Salian, A. S. (2003), 'A high-sensitivity silicon accelerometer with a folded-electrode structure.', *Journal of Microelectromechanical Systems* **12**(4), 479–486.

Nelder, J. and Mead, R. (1965), 'A simplex method for function minimization', *Comput Journal* **4**, 308–313.

Paros, J. and Weisbord, L. (1965), 'How to design flexure hinges', *Machine Design* **37**, 151–156.

Pedersen, P. (2007), Some benchmarks for optimized shapes with stress concentration, *in* '7th World Congress on Structural and Multidisciplinary Optimization', Seaoul, Korea, pp. 1623–1631.

Pilkey, W. D. (2005), *Formulas for Stress, Strain, and Structural Matrices*, 2nd edn, John Wiley & Sons, Inc.

Puers, R. and Reyntjens, S. (1998), 'Design and processing experments of a new miniaturized capacitive triaxial accelerometer', *Sensors and Actuators* **A**(68), 324–328.

Rahman, M. (2006), 'An intelligent moving object optimization algorithm for design problems with mixed variable, mixed constraints, and multiple objectives', *Structural Multidisciplinary Optimization* **32**, 40–58.

Roark, R. J. and Young, W. C. (1975), *Formulas for Stress and Strain.*, 5nd edn, McGraw-Hill.

Senturia, S. (2001), *Microsystem Design*, 3nd edn, Kluwer Academic Publishers, Boston, USA.

Stuart, S., Vivek, B., Jami, D. and Ying, X. (1997), 'Elliptical flexure hinges', *Review of Scientific Instruments* **68**(3), 1474–1483.

Suna, C., Wang, C. and Fang, W. (2008), 'On the sensitivity improvement of cmos capacitive accelerometer.', *Sensors and Actuators* **A**(141), 347–352.

Werme, M. (2007), Designing compliant mechanisms with stress constraints using sequential linear integer programming, *in* '7th World Congress on Structural and Multidisciplinary Optimization', Seaoul, Korea, pp. 1862–1871.

Williams, M. (1952), 'Stress singularities resulting from various boundary conditions in angular corners of plates in extension.', *Journal of Applied Mechanics* **74**, 526–528.

Yingfei, W. and Zhaoying, Z. (2002), 'Design calculations for flexure hinges', *Review of Scientific Instruments* **73**(8).

Document Log:

Manuscript Version 0

Typeset by $\mathcal{AMS}$-LaTeX — 6 January 2009

SIMON DESROCHERS

CENTRE FOR INTELLIGENT MACHINES, MCGILL UNIVERSITY, 3480 UNIVERSITY ST., MONTREAL (QUÉBEC), H3A 2A7, CANADA

E-mail address: `simond@cim.mcgill.ca`

Typeset by $\mathcal{AMS}$-LaTeX